International Journal of Thermofluids 22 (2024) 100683

Contents lists available at ScienceDirect

International Journal of Thermofluids

journal homepage: www.sciencedirect.com/journal/international-journal-of-thermofluids

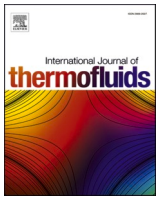

Multi-scale modelling of boiling heat transfer: Exploring the applicability of an enhanced volume of fluid method in sub-micron scales

Bhaskar Chakraborty [a,*], Mirko Gallo [a,b], Marco Marengo [a,c], Joel De Coninck [a], Carlo Massimo Casciola [b], Nicolas Miche [a], Anastasios Georgoulas [a]

[a] School of Architecture, Technology and Engineering, Advanced Engineering Centre, University of Brighton, Brighton, UK
[b] Department of Mechanical and Aerospace Engineering, La Sapienza University of Rome, Rome, Italy
[c] Department of Civil Engineering and Architecture, University of Pavia, Pavia, Italy

ARTICLE INFO

Keywords:
VOF
Boiling
Multi-scale modelling

ABSTRACT

The advancement of technology has led to a significant increase in thermal loads, thus presenting new challenges in heat dissipation. Traditional single-phase cooling systems are often inadequate to meet these demands. As a result, phase-change technologies utilizing boiling and condensation, which can achieve high heat transfer coefficients, have garnered considerable attention. To delve into the complex physics of boiling heat transfer, researchers are increasingly turning to numerical simulation methods such as the Volume of Fluid (VOF) and the Diffuse Interface (DI) approaches. The VOF method, widely employed for macro-scale simulations ranging from micrometers to millimeters, effectively tracks bubble growth and detachment. Conversely, the DI method represents the interface as a continuous phase field and is primarily used for mesoscale simulations spanning from nanometers to micrometers. While the DI method excels in resolving mesoscale interfacial phenomena, it is computationally expensive for larger domains. Considering the strengths and weaknesses of both the VOF and DI methods, there is a growing interest in developing a multi-scale modeling approach that amalgamates their benefits. To pursue this objective, initial efforts are being made to evaluate the scaling capability of VOF towards lower spatial and temporal limits. Hence, an enhanced and customized VOF methodology has been developed within the OpenFOAM toolbox. This methodology is employed to investigate various bubble growth scenarios, progressively exploring its applicability at lower temporal and spatial scales to identify the lower limits of its application. By taking this first step towards combining the strengths of both the VOF and DI methods through a multi-scale modeling approach, the presented paper paves the way for enhancing the accuracy and efficiency of modelling approaches for boiling heat transfer while tackling a challenge associated with varying spatial and temporal scales. This endeavor not only pushes the boundaries of computational fluid dynamics but also holds promise for addressing real-world thermal management issues in diverse technological applications.

1. Introduction

Boiling heat transfer is a crucial aspect of both everyday life and industrial applications, and its study involves a deep understanding of its underlying nature. This knowledge is essential for the design and optimization of various thermal systems and technologies. The study of boiling heat transfer covers a broad range of spatial and temporal scales, which makes it complex and diverse. This diversity in scale and application contexts makes it challenging to generalize operating conditions, leading to extensive and ongoing research in this field. Research groups worldwide continue to investigate boiling heat transfer to enhance our understanding and application of this phenomenon. This ongoing research is vital because it contributes to advancements in numerous fields, including energy production, electronics cooling, and other industrial processes. Understanding the nuances of boiling heat transfer enables engineers and scientists to develop more efficient, reliable, and sustainable systems. Such research on boiling heat transfer not only improves existing cooling technologies but also paves the way for new innovations that can have a significant impact on various sectors.

In the literature, various semi-empirical correlations have been presented based on several experiments for different parameter ranges. However, the number of influencing parameters is very high and is further increased by new experiments deploying new experimental

* Corresponding author.
E-mail address: B.Chakraborty@brighton.ac.uk (B. Chakraborty).

https://doi.org/10.1016/j.ijft.2024.100683

Available online 30 April 2024

Nomenclature

c_p	Specific heat capacity ($J/kg/K$)
C_γ	coefficient, multiplier to volumetric flux
C_{pv}	Heat capacity for vapor (J/K)
C_{pl}	Heat capacity for liquid (J/K)
D	Diffusion constant (m^2/s)
F	Force per unit volume ($kg/m^2/s^2$)
F_{ST}	Surface tension force ($kg/m^2/s^2$)
F_g	Gravitational force ($kg/m^2/s^2$)
h	Height (m)
h_{lv}	Latent heat of evaporation (J/kg)
$\dot{h}$	Energy source term (W/m^3)
j_{evap}	Mass flux at the interface (kg/m^2K)
L	Length (m)
L_0	Characteristic length (m)
$\dot{m}_{int}$	Mass flow from liquid to vapor (kg/s)
n_f	Cell surface normal vector
N_l	Scaling factor for liquid
N_v	Scaling factor for vapor
p/P	Pressure ($kg/m\text{-}s$)
$\dot{q}$	Heat flux (W/m^2)
R_{int}	Interfacial heat resistance (K^2s^2/kg)
R_{gas}	Specific gas constant ($J/K-mol$)
$R(t)$	Bubble radius (m)
R_0	Initial radius (m)
r	Radius (m)
t	Time (s)
t_0	Characteristic time (s)
T	Temperature (K)
T_{int}	Temperature at the interface (K)
T_{sat}	Saturation temperature (K)
T_∞	Bulk temperature (K)
S_f	Surface area of the cell (m^2)
t	Time (s)
U	Velocity (m/s)
U_r	Artificial Compression velocity (m/s)

Greek symbols

α	Volume fraction
$\widetilde{\alpha}$	Smoothed volume fraction
β	Growth constant
δ_{therm}	Thermal Boundary Layer
τ	Artificial time step (s)
α_f	Smoothed volume fraction at cell face
$\widetilde{\alpha}_p$	Smoothed volume fraction at cell center
ρ	Density (kg/m^3)
θ_{Wedge}	Angle ($^\circ$)
θ_a	Advancing contact angle ($^\circ$)
θ_r	Receding contact angle ($^\circ$)
$\dot{\rho}$	Rate of change of density (kg/m^3-s)
σ	Surface tension (N/m)
μ	Dynamic viscosity ($kg/m\text{-}s$)
λ	Thermal conductivity ($W/m\text{-}K$)
φ	Volumetric flow rate (m^3/s)
ω	Uncertainty parameter, $0 < \omega < 1$
$\dot{\rho}_0$	Rate of change of density (kg/m^3-s)
$\dot{\rho}_1$	Rate of change of density (kg/m^3-s)
γ	Bulk properties
γ_l	Bulk properties for liquid
γ_v	Bulk properties for vapor
κ	Interface curvature (m^{-1})

Superscript

T	Transpose

Subscript

ST	Surface Tension
g	Gravity
f	Face
p	Cell center
0	Initial condition
1	First time interval
cut	Cut-off value
l	Liquid
v	Vapor

correlations [1]. Therefore, in order to get a further improvement in the existing predictive tools, a deeper physical understanding of the boiling processes for the various temporal and spatial scales is necessary [2]. A thorough physical comprehension of boiling phenomena can typically be attained through either detailed boiling experiments or precise numerical simulations. These methodologies should not be seen as isolated or in opposition to each other. Instead, they ought to be employed in tandem. This integrated approach enables quantitative comparisons and enhances the ability to design effective thermal systems. Utilizing both highly resolved experimental data and advanced simulations together provides a more complete picture, facilitating better understanding and optimization in the field of boiling heat transfer.

However, as computing power increases and resources become more abundant, coupled with swift advancements in modern numerical methods for multi-phase flow simulation, the numerical simulation of boiling heat transfer has become feasible across various applications and scales, both spatially and temporally. In recent times, Computational Fluid Dynamics (CFD) codes have expanded to encompass the analysis of three-dimensional, multi-phase flows. This development aims to address the limitations of one-dimensional numerical models. Presently, the literature on the numerical study of boiling heat transfer using CFD typically branches into three main categories, that are nano-scale, meso-scale, and macro-scale simulations.

To study boiling at the nano-scale of the spatial arrangement, the technique of Molecular Dynamics (MD) simulation is employed and is used for simulating nucleation by many researchers. In the work of Hens et al. bubble nucleation on the surface of smooth substrates at inhomogeneous temperatures has been studied [3]. The observed results implied that bubble nucleation could be seen in the region with higher temperature. Nagayama et al. [4] have also studied the bubble nucleation behavior at the nanoscale. They found that the nucleation behavior of bubbles was varied significantly on smooth substrates with different wettability. In the research of Maruyama et al. [5] a study has been performed for heterogeneous nucleation at the wall surface by changing the interfacial wettability. It was observed that the ratio of contact angle to the bubble radius is a linear function of the depth of the effective surface potential for the liquid bubble surface. In the work of Yamamoto et al. [6] the initial stages of bubble nucleation on smooth substrates were studied. The investigation was performed for early stages of bubble nucleation on smooth substrates with inhomogeneous superheat and surface wettability, respectively. Under these two conditions, bubble nucleation was successfully generated near the substrate. At the vicinity of the substrate, the nucleation time was related to the wettability and superheat of the substrate. The bubble nucleation inception for liquid argon at different temperatures and wettability surfaces was studied by Zhou et al. [7]. The authors found that at lower wall temperatures, bubbles tended to nucleate first in the hydrophobic part of the wall. Alternatively, with the rise of the wall temperature, the

position of bubble nucleation shifts from the hydrophobic region to the hydrophilic region. In the work of Chen et al. [8] a molecular dynamics simulation was used to analyze the position of bubble nucleation for liquid argon. It was observed that the nucleation first forms in the vicinity of a groove region. This is a consistent conclusion with respect to the classical non-homogeneous nucleation theory. The MD simulation method is a powerful tool to study the phase transition processes of polyatomic molecules such as water at the nanoscale [9–13]. However, it requires a prohibitive computational cost [14]. So, this requirement can be sufficed by using meso-scale simulations instead. In this respect, Gallo et al. proposed to address vapor bubble nucleation with a mesoscale method based on fluctuating hydrodynamics combined with a diffuse interface model, both in homogeneous [15] and heterogeneous conditions [16]. Diffuse interface approaches are particularly useful for describing in a thermodynamically consistent way physical systems at the mesoscale comprising micro/nano bubbles [17–19], liquid films and interfaces [20,21], fluid membranes [22,23] and crystals [24]. For small fluctuations, fluctuating hydrodynamics enforces the Einstein-Boltzmann equilibrium distribution in Navier-Stokes dynamics [25].

The afore mentioned coupling results in a set of stochastic partial differential equations extending Landau and Lifshitz's fluctuating hydrodynamic theory for capillary fluids. In [15] the authors studied the bubble nucleation in metastable liquids and favorably compared the nucleation rate with MD simulations. Later, in [16], the authors extended their work from a homogeneous scenario and studied heterogeneous nucleation dynamics on a surface. The technical aspect of the work was to directly account for hydrophobic or hydrophilic walls through appropriate boundary conditions compliant with the fluctuation-dissipation balance. The proposed Fluctuating Diffuse Interface (FDI) methodology provided access to the complete dynamics of the nucleation process, from the inception of multiple bubbles up to their long-time macroscopic expansion, on time and spatial scales that are unaffordable by molecular dynamics. The analysis mainly focused on the effect of wall wettability, on the nucleation rate, and, qualitatively in agreement with classical nucleation theory predictions, it revealed several discrepancies to be ascribed to layering effects in the liquid close to the boundary and bubble–bubble interactions. It was found that close to moderately hydrophilic surfaces; the most probable nucleation event occurs away from the wall through a homogeneous type mechanism.

The same model has been employed in [26] to investigate the boiling inception on a smooth surface. In this work, the role of sub-critical bubble embryo interaction to enhance bubble nucleation was detected. In more detail, a small vapor bubble embryo can survive longer than expected due to coalescence events with neighboring embryos. In another work, Gallo et al. [27], proposed a coarse-grained version of the isothermal diffuse interface model, that is obtained through the averaging of the complete three-dimensional equations on spherical shells. The resulting stochastic equations spatially depend on the radial distance from the vapor cluster center. An analogous procedure was also employed to study the statistical properties of thermal fluctuations in capillary fluids [28].

Finally, in the latest work by Gallo et al. [29], a dynamical theory of boiling based on fluctuating hydrodynamics and the diffuse interface approach is presented. The utilized mesoscale model was able to describe pool boiling scenarios from the stochastic nucleation up to the macroscopic bubble dynamics. Furthermore, the methodology extracts a modest computational cost to analyses and study using the proposed mesoscale technique from nano to micrometers, where most of the controversial observations related to the investigated phenomenon originate. Additionally, the role of wettability in the macroscopic observables of boiling is studied. Furthermore, the ideal case of boiling on ultra-smooth surfaces with a chemically heterogeneous wall was also simulated, and the results were comparable with the onset temperatures observed in experiments. As mentioned earlier the proposed mesoscale simulation method that utilizes the diffuse interface approached with fluctuating hydrodynamics can capture the physics from nano to micrometers, however, for the analysis of higher scales such as in the range of micrometers to hundreds of millimeters, macro-scale analysis tools are required, since mesoscale simulations become computationally intensive for higher scales.

Macro-scale scenarios are usually analyzed by interface capturing methods such as the Volume of Fluid (VOF) or Level-Set (LS) method. The LS method captures a sharp interface of evaporating bubbles utilizing a distance function from the interface; however, due to required re-initialization steps of this distance function it lacks mass conservation. On the other hand, VOF has exceptional mass conserving characteristics [30–33], and is used significantly studying boiling phenomena [34–37]. In boiling flows, the interface between liquid and vapor undergoes significant topological changes, such as the formation and collapse of bubbles. VOF can handle these complex changes efficiently, ensuring accurate simulations of the boiling dynamics. Therefore, the VOF method can be considered as the most popular interface-capturing approach [37]. In the work of Welch and Rachidi [38], the VOF model of Welch and Wilson [39] is extended by adding transient heat conduction in the solid wall and simulated film boiling. The nucleate pool boiling of water is simulated using VOF method by Aus der Wiesche [40]. Hardt and Wondra [41] developed a method for implementing phase change in a VOF or LS approach and performed simulations of film boiling and droplet evaporation using a VOF methodology. Ose and Kunugi [42,43] performed simulation of sub-cooled pool boiling and validated the numerical results using their own qualitative experimental data. In the work of Kunkelmann et al. [44] an extension of a specific sub-model for micro-layer evaporation is carried out that had been previously developed, and is coupled with a user-defined diabatic VOF solver of the open-source CFD package OpenFOAM [45]. A more elaborated information on the developed numerical method is available in Kunkelmann's PhD thesis [46]. Furthermore, a VOF-based sharp-interface phase change model has been demonstrated in the work of Sato and Niceno [47], where a Conservative Semi Lagrangian Constrained Interpolation Profile method (CIP-CSL) was used to solve the advection equation of the color function. Georgoulas et al. [37] have also presented an Enhanced VOF Method coupled with heat transfer and phase-change to characterize bubble detachment in saturated pool boiling conditions. In their work they have validated their developed customized OpenFOAM solver against analytical benchmarks as well as experimental measurements from the literature. The same research group has then further developed their numerical simulation framework in OpenFOAM adding a more accurate dynamic contact angle model for wettability effects as well as conjugate heat transfer between solid and two-phase flow domains and they applied it to a wide series of investigations focused on flow boiling within micro passages [48–54].

All the above mentioned VOF-based numerical investigations are usually applied for scales ranging from hundreds of μm up to tens of millimeters and they require the artificial patching of a single or multiple artificial bubble embryos on a heated wall for the boiling process to initiate without physically or empirically accounting for nucleation. It is therefore evident that a multi-scale modelling approach should be developed and adopted in order to be able to accurately predict bubble dynamics and boiling heat transfer characteristics, where VOF-based methods can be coupled with mesoscale methods in order to physically account for all the stages of boiling process, starting from bubble nucleation at the nanoscale up to the bubble growth, detachment and bubble to bubble interaction at the micro to millimetric scales.

As a first step in this direction, in the present work, the enhanced VOF-based method of Georgoulas et al. [37] that accounts for spurious currents reduction (a well-known drawback of VOF-based methods), enhanced dynamic contact angle modelling for accurate capturing of wettability effects as well as for boiling and condensation is further employed for the simulation of key boiling benchmarks such as the growth of vapor bubbles in superheated liquid domains as well as for more realistic boiling phenomena such as the formation, growth and

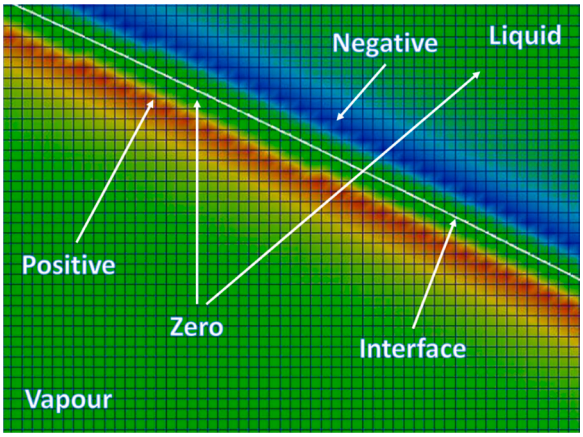

Fig. 1. Distribution of the final source terms in the computational domain for the case of an evaporating bubble [37].

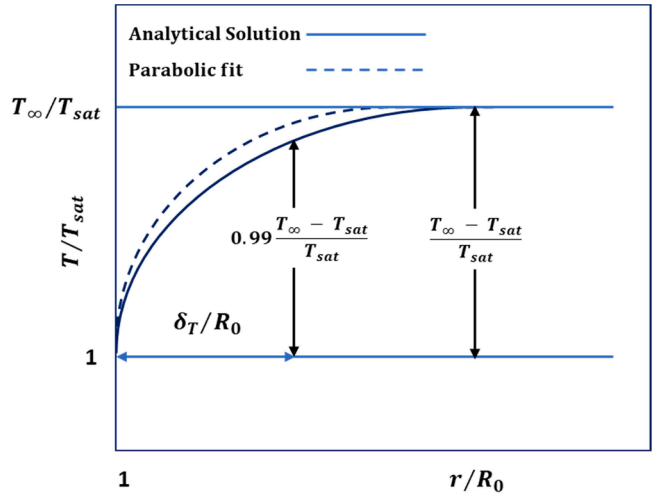

Fig. 2. Initial dimensionless temperature profile at the bubble interface on the liquid side.

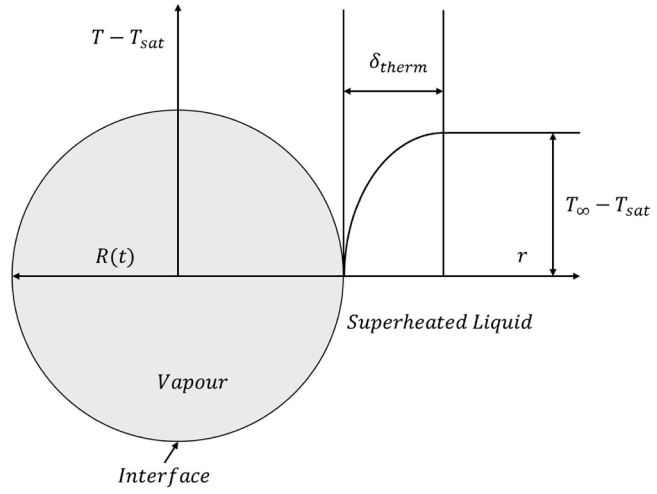

Fig. 3. Schematic illustration of the geometrical characteristics and the initial conditions of the simulated validation cases.

detachment of single vapor bubble embryos from superheated plates of variable wettability characteristics in saturated pool boiling conditions. The particular focus of the present work however is to explore the applicability of the proposed VOF-based numerical simulation framework to sub-micron level spatial scales providing critical insights into the prediction of boiling heat transfer characteristics, approaching the precision and upper applicability limits of the FDI mesoscale modelling approach. The findings demonstrate that the utilized enhanced VOF method is effective and accurate even at such smaller scales, pushing beyond the traditional boundaries of scale limitations. This novel attempt paves the way for future coupling of the proposed VOF method with the FDI method that was previously mentioned, with the future potential of leading to a comprehensive, multi-scale modeling framework that can accurately replicate boiling heat transfer at all necessary scales, physically accounting for bubble nucleation, growth, and detachment.

2. Numerical method

2.1. Governing equations

In this section, the key equations governing mass, momentum, energy, and volume fraction are outlined for the proposed VOF method. Notably, both the liquid and vapor phases are considered incompressible and treated as Newtonian fluids. While the incompressibility of the liquid phase is evident, the vapor phase also qualifies for this treatment. This is because the highest flow velocity observed in the vapor phase remains within a few meters per second. As a result, the Mach number remains sufficiently low, allowing us to disregard the effects of compressibility and treat both phases as incompressible.

The mass conservation equation is given as:

$$\nabla\cdot\left(\rho\vec{U}\right) = \dot{\rho} \tag{1}$$

Where U is the fluid velocity and ρ is the bulk density. The source term on the right-hand side accounts for the phase change [37]. It should be mentioned that despite the local source terms, the mass is globally conserved since all the mass that is removed from the liquid side of the interface is added on the vapour side.

The conservation of momentum is given by the following equation:

$$\frac{\partial\left(\rho\vec{U}\right)}{\partial t} + \nabla\cdot\left(\rho\vec{U}\vec{U}\right) - \nabla\cdot\left\{\mu\left[\left(\nabla\vec{U} + \left(\nabla\vec{U}\right)^T\right)\right]\right\} = -\nabla p + \vec{F}_{ST} + \vec{F}_g \tag{2}$$

Where p is the pressure and μ is the bulk dynamic viscosity. The momentum source terms on the right-hand side of the equation account for the effects of surface tension and gravity, respectively. The surface tension term is modelled according to the classical approach of Brackbill et al. [55].

The conservation of energy balance is given by the following equation:

$$\frac{\partial(\rho c_p T)}{\partial t} + \nabla\cdot\left(\vec{U}\rho c_p T\right) - \nabla\cdot(\lambda\nabla T) = \dot{h} \tag{3}$$

where c_p is the bulk heat capacity, T is the temperature field, and λ is the bulk thermal conductivity.

The source term on the right-hand side of the equation will be explained in next section is linked to the phase-change during boiling and/or condensation.

The volume fraction α is advected by the flow field using the following equation:

$$\frac{\partial\alpha}{\partial t} + \nabla\cdot\left(\alpha\vec{U}\right) - \nabla\cdot(\alpha(1-\alpha)U_r) = \frac{\dot{\rho}}{\rho}\alpha \tag{4}$$

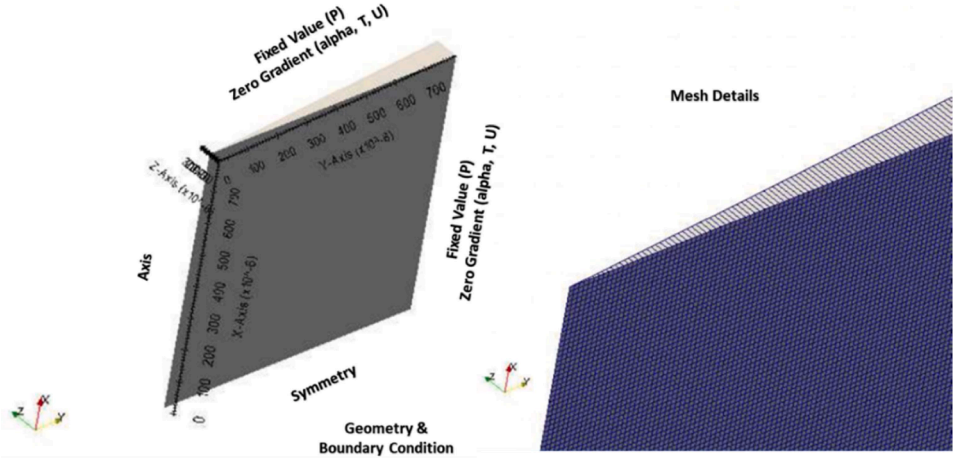

Fig. 4. Two-dimensional axisymmetric computational domain, mesh, and boundary conditions. An 800 μm x 800 μm 5°-wedge domain was utilized, with a uniform cell size of 0.5 μm.

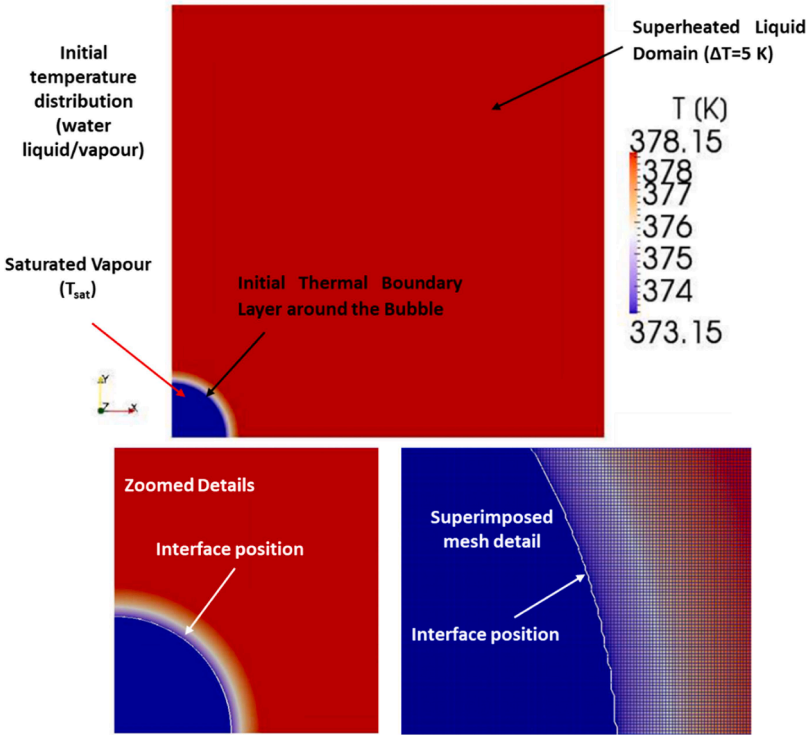

Fig. 5. Initial conditions for the water liquid/vapor: P_{sat} = 1.013 bar, 5 K of liquid superheat.

Interface sharpening is very important in simulating two-phase flows of two immiscible fluids. In OpenFOAM, the sharpening of the interface is achieved artificially by introducing the extra compression term in Eq. (4) ($\nabla \cdot (\alpha(1-\alpha)U_r)$), where U_r is the artificial compression velocity which is calculated from the following relationship:

$$U_r = n_f \min\left[C_\gamma \frac{|\varphi|}{|S_f|}, \max\left(\frac{|\varphi|}{|S_f|}\right)\right] \quad (5)$$

where n_f is the cell surface normal vector, φ is the volumetric flow rate, S_f is the surface area of the cell, and C_γ is a coefficient the value of which can be set between 1 and 4. Then U_r is the relative velocity between the two fluid phases due to the density and viscosity change across the interface. In Eq. (4), the divergence of the compression velocity U_r ensures the conservation of the volume fraction α, while the term $\alpha(1-\alpha)$ limits this artificial compression approach only in the vicinity of the interface, where $0 < \alpha < 1$ [56]. The level of compression depends on the value of C_γ [56,57]. For the simulations of the present investigation, initial trials indicated that a value of $C_\gamma = 1$ should be used in order to maintain a quite sharp interface; the model generates non-physical results for values greater than 1, as it was observed that it loses realistic curvature values in comparison to experimental results [58]. The source term on the right-hand side of the Eq. (4) is needed because, due to the local mass source terms, the velocity field is not free of divergence.

It should be mentioned that the VOF method in OpenFOAM does not solve Eq. (4) implicitly, but instead by applying a multidimensional universal limiter with an explicit solution algorithm (MULES). Together with the interface compression algorithm, this method ensures a sharp interface and bounds the volume fraction values between 0 and 1 [59]. The volume fraction values greater than 1 and less than 0 generates unphysical values for bulk properties.

Table 1
Material properties and initial conditions for the numerical simulations (validation cases).

Property	Unit	Water		R134a		FC-72	
		Liquid	Vapor	Liquid	Vapor	Liquid	Vapor
Density (ρ)	(kg/m^3)	957.45	0.62	1388.00	4.43	1621.20	13.49
Specific heat capacity (c_p)	(J/kg/K)	4220	2085	1270	720	1106	925
Thermal conductivity (k)	(W/m/K)	0.677	0.025	0.106	0.009	0.054	0.014
Dynamic viscosity (μ)	(Pa-s)	2.78e-4	1.23e-5	4.01e-4	9.64e-6	4.13e−4	1.19e−5
Heat of vaporization (h_{lv})	(J/kg)	2,253,100		219,500		83,562	
Surface tension (σ)	(N/m)	0.059		0.016		0.008	
Saturation temperature (T_{sat})	(K)	373.15		303.15		330.06	
Pressure (P)	(bar)	1.059		0.840		1.013	
Growth Constant (β)	(-)	14.59		8.75		7.69	
Initial thermal layer thickness (δ_{therm})	(m)	28.00 × 10^{-6}		22.00 × 10^{-6}		26.00 × 10^{-6}	
Superheat (ΔT)	(K)	5		5		5	

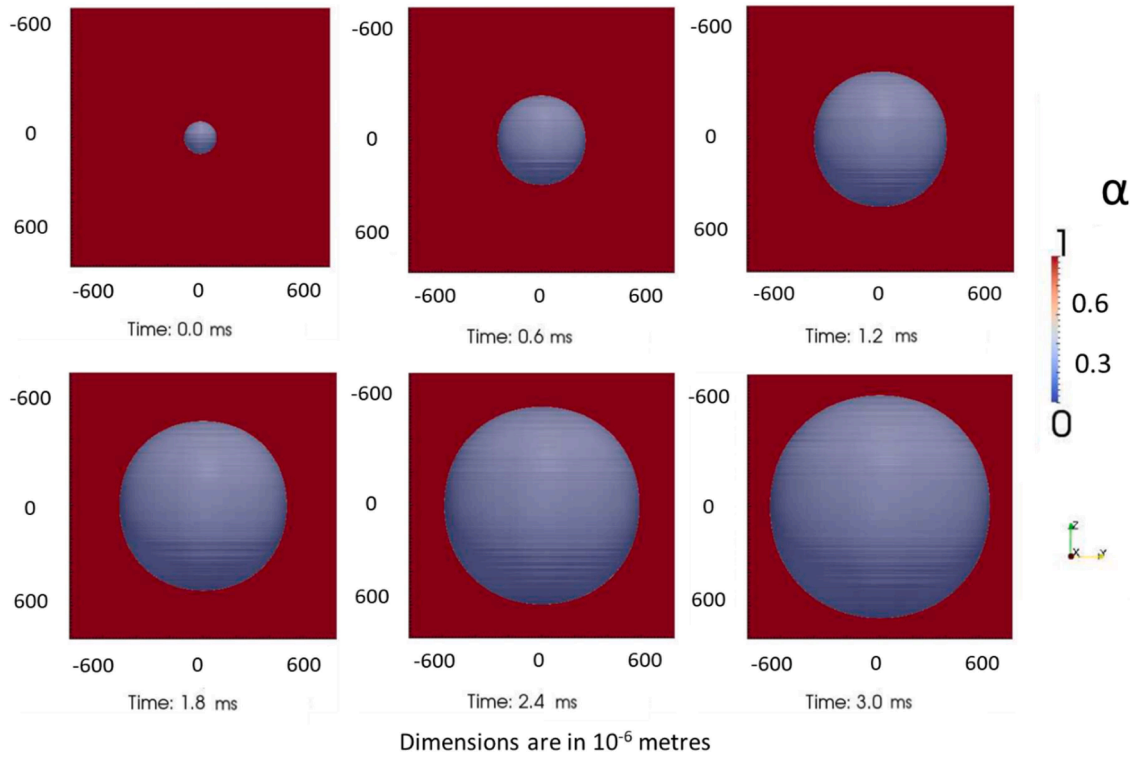

Fig. 6. Bubble evolution with time for the water liquid/vapor simulation for Large Scale case (Typical scale: initial bubble radius R_o=100 μm, 800 μm x 800 μm domain), α denotes the volume fraction of the liquid.

Finally, the bulk fluid properties γ are computed as the averages over the liquid (γ_l) and vapor (γ_v) phases, weighted with the volume fraction α:

$$\gamma = \alpha\gamma_l + (1-\alpha)\gamma_v \tag{6}$$

As it is known, the VOF method usually suffers from non-physical spurious currents in the interface region. These spurious velocities are due to errors in the calculation of the normal vectors and the curvature of the interface that are used for the calculation of the interfacial forces. These errors emerge from the fact that in the VOF method, the interface is implicitly represented by the volume fraction values that encounter sharp changes over a thin region [60].

As previously mentioned in the introduction section of the present paper, the VOF-based solver that is used in the present investigation has been modified accordingly in order to account for an adequate level of spurious current suppression. The proposed modification involves the calculation of the interface curvature κ using smoothed volume fraction values $\widetilde{\alpha}$ which are obtained from the initially calculated volume fraction field α, smoothing it over a finite region in the vicinity of the interface:

$$\kappa = \nabla\cdot\left(\frac{\nabla\widetilde{\alpha}}{|\nabla\widetilde{\alpha}|}\right) \tag{7}$$

All other equations are using the initially calculated (non-smoothed) volume fraction values of α. The proposed smoothing is achieved by the application of a smoothing filter [61] which can be described by the following equation:

$$\widetilde{\alpha}_p = \frac{\sum \alpha_f S_f}{\sum S_f} \tag{8}$$

In Eq. (8), the subscripts p and f denote the cell and face index, respectively, and α_f is the linearly interpolated value of α at the face center. The smoothed volume fraction is evaluated as the ratio of the summation of the cell face area weighted volume fraction to the summation of the cell face area. The application of the proposed filter can be repeated more than one time in order to obtain an adequately smoothed

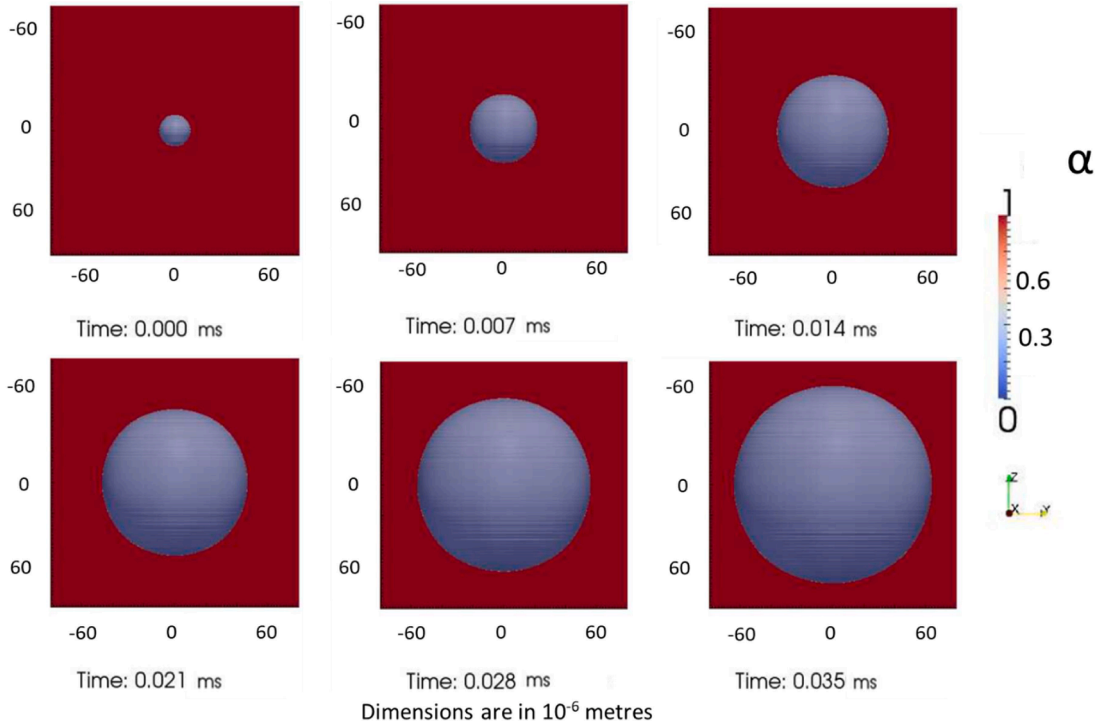

Fig. 7. Bubble evolution with time for the water liquid/vapor simulation for Medium Scale case (scaled down by a factor of 10: initial bubble radius R_o=10 μm, 80 μm x 80 μm domain), α denotes the volume fraction of the liquid.

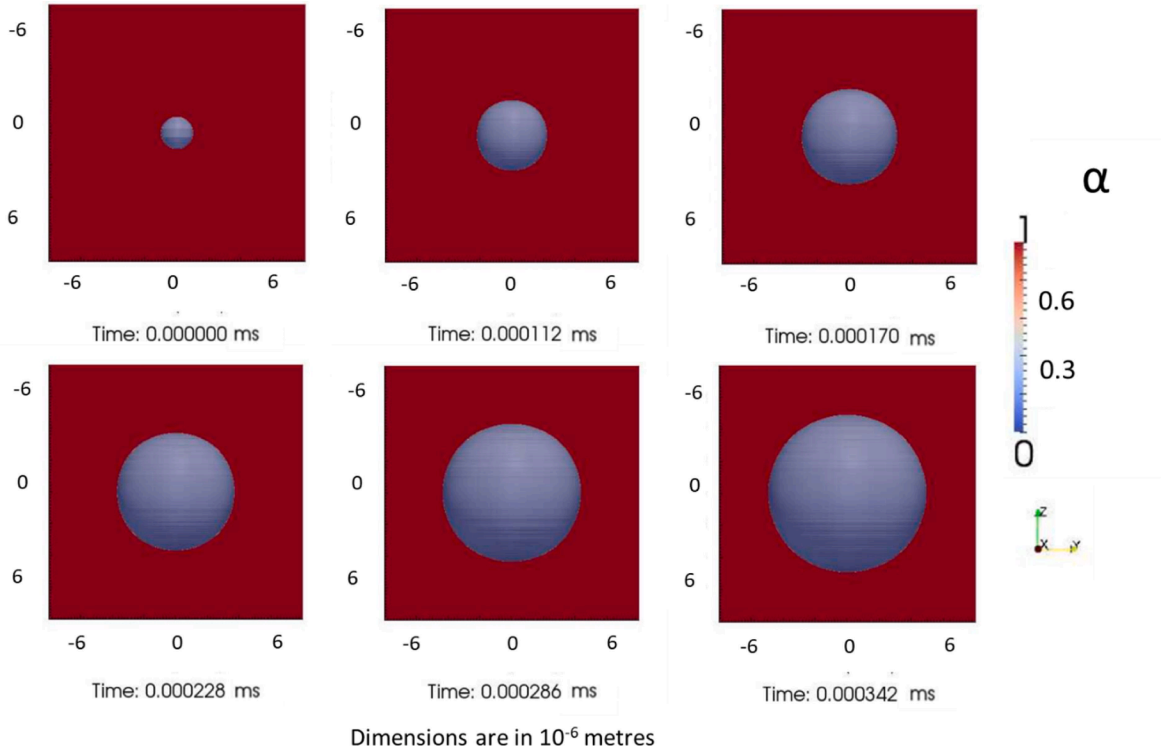

Fig. 8. Bubble evolution with time for the water liquid/vapor simulation for Small Scale case (scaled down by a factor of 100: initial bubble radius R_o=1 μm, 8 μm x 8 μm domain), α denotes the volume fraction of the liquid.

field. For the applications of the present investigation, initial trial simulations indicated that the filter should be applied no more than two times. If the smoothing filter is applied only once it still leaves a significant amount of spurious currents in the interface region. Additional application of the smoothing filter for more than 2 times, will significantly suppress spurious currents but it will also level out high curvature regions that will eventually lead to non-physical results. The proposed, enhanced VOF solver has been tested and verified against experimental results of isothermal bubble dynamics available in the literature with an excellent degree of convergence. More details on the

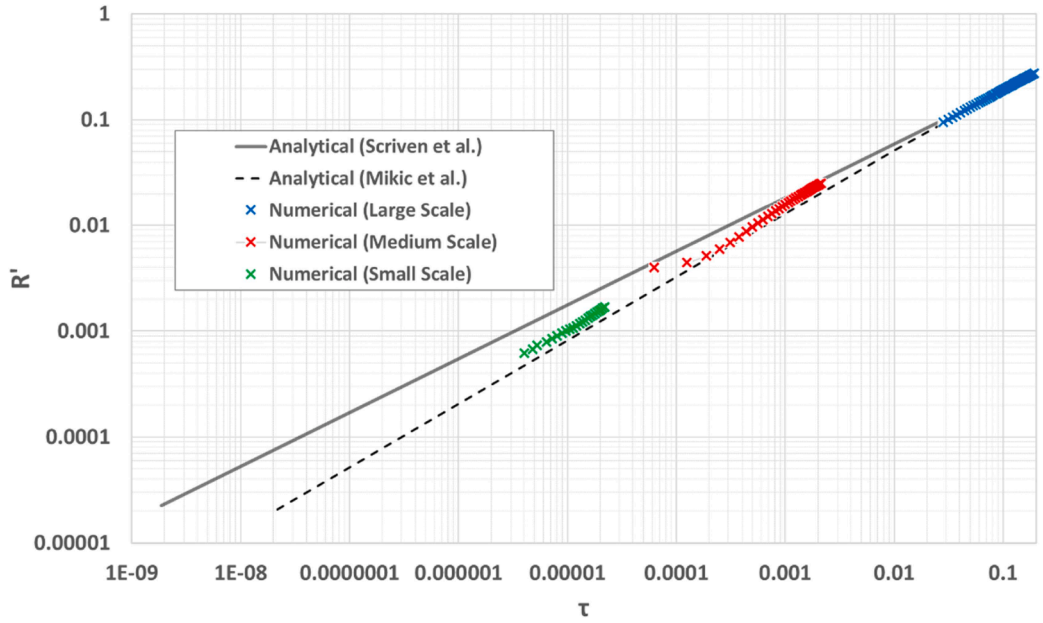

Fig. 9. Bubble growth characteristics for different scales (water).

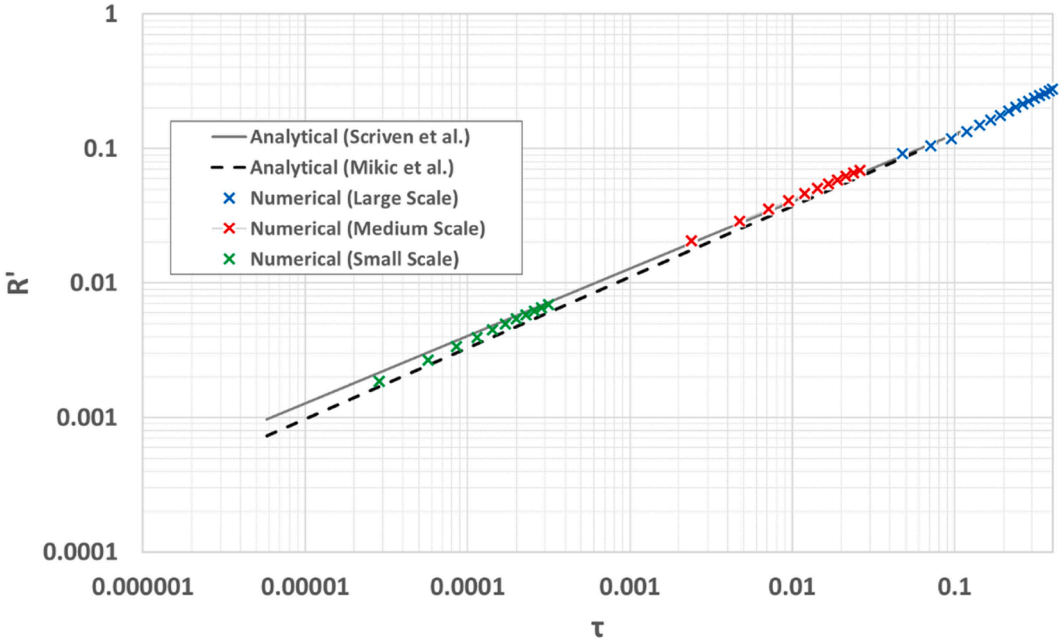

Fig. 10. Bubble growth characteristics for different scales (R134a).

proposed validation as well as on the proposed improved VOF method can be found in the paper by Georgoulas et al. [58].

2.2. Phase change model

The utilized phase change model which was implemented in the improved OpenFOAM VOF solver that is used in the present investigation will be described briefly in this section. Supplementary details can be found in the work of Georgoulas et al. [37].

The evaporating mass flux at the liquid-vapor interface j_{evap} is calculated from the following equation:

$$j_{evap} = \frac{T_{int} - T_{sat}}{R_{int} h_{lv}} \tag{9}$$

where T_{int} is the temperature of the interface, T_{sat} is the saturation temperature, R_{int} is the interfacial heat resistance and h_{lv} is the latent heat of evaporation at the saturation temperature.

The interfacial heat resistance is calculated by the following equation based in the considerations of Schrage [62],

$$R_{int} = \frac{2 - \omega}{\omega} \frac{\sqrt{2\pi R_{gas}}}{h_{lv}^2} \frac{T_{sat}^{3/2}}{\rho_v} \tag{10}$$

It is clear, that this last equation is in fact a fitting function, due to the uncertainty of the parameter ω, which eventually may vary in the range $0 < \omega < 1$. For the cases that will be presented here, the constant ω which is also known as the evaporation/condensation coefficient is taken equal to unity from a previous validation utilizing the same solver [37] and is also in agreement with other previous works in the literature [45,46,44,

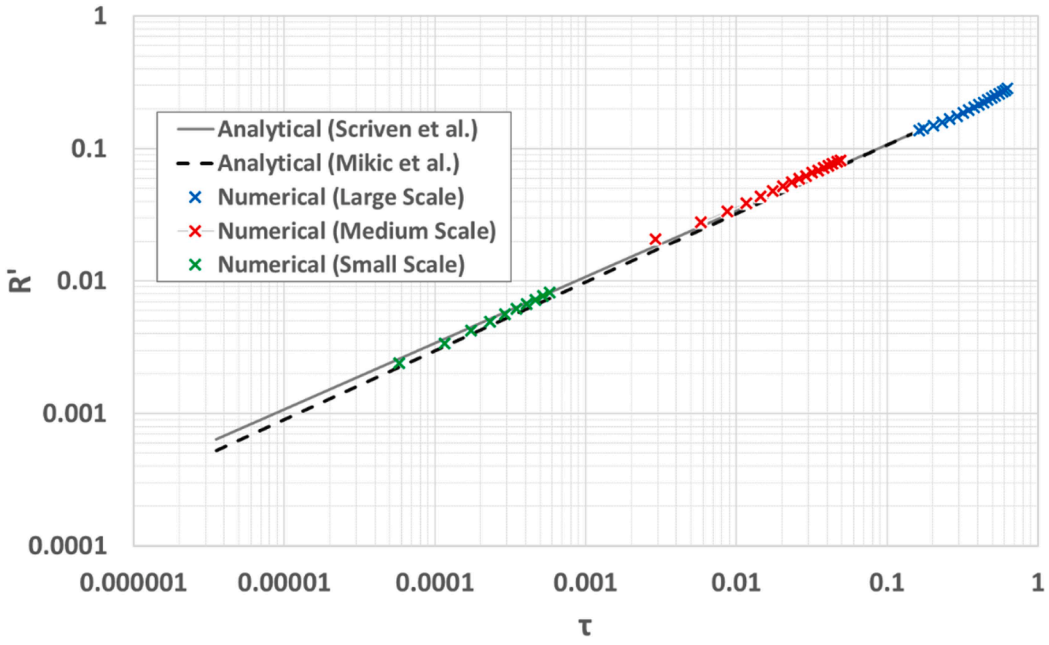

Fig. 11. Bubble growth characteristics for different scales (FC72).

Table 2
Quantitative % deviation range for Scriven and Mikic analytical solution.

	Range of % deviation from Scriven et al.	Range of % deviation from Mikic et al.
Water Large Scale	1.29–4.23	2.73–5.99
Water Medium Scale	8.06–29.44	2.19–12.76
Water Small Scale	1.62–38.23	0.83–3.98
R134a Large Scale	1.19–8.23	0.86–8.62
R134a Medium Scale	4.78–17.92	3.22–25.17
R134a Small Scale	2.66–18.98	0.58–21.96
FC72 Large Scale	1.39–5.51	0.20–5.33
FC72 Medium Scale	1.67–4.64	0.31–2.17
FC72 Small Scale	6.90–11.12	3.49–6.32

63,]. However, it should be noted that in different cases that are not presented in the present investigation (i.e. in condensation heat transfer cases), the value of the proposed coefficient needed to be significantly lower than unity. R_{gas} is the specific gas constant of the working fluid that is calculated from the universal gas constant and the molecular weight of the working fluid. The amount of liquid that evaporates is calculated locally and the resulting source term field is smeared over a few cells in order to avoid numerical instabilities. The evaporating mass is taken away on the liquid side of the interface and reappears on the vapour side. According to previous investigations [37,45,46,44,63,], even though Eqs. (9) and (10) are derived from considerations on length scales which are several orders smaller than the typical grid size used in the simulations, the proposed evaporation model leads to correct evaporation rates since it acts as a control loop. The more the temperature at the interface deviates from the saturation value, the more liquid evaporates and the more the temperature drops locally. This ensures that the temperature at the liquid-vapor interface always remains close to the saturation temperature.

The evaporating/condensing mass flux is calculated from Eq. (9) and must be incorporated into the conservation equations, by the definition of volumetric source terms. This is done by multiplying the evaporating mass flux at the liquid-vapor interface by the magnitude of the volume fraction gradient, as indicated in the following equation:

$$\dot{\rho}_0 = j_{evap}|\nabla\alpha| \tag{11}$$

This initial sharp source term field (SSTF) is integrated over the whole computational domain to calculate the "Net Mass Flow" through the entire liquid-vapor interface, using the following equation:

$$\dot{m}_{\text{int}} = \int\int\int \dot{\rho}_0 dV \tag{12}$$

This value is important for global mass conservation, in order to ensure that the magnitudes of the mass sources in the liquid and vapor parts are equal and correspond to the net evaporation rate. The sharp source term field is then artificially smeared over several cells, by solving the following diffusion equation for the smooth distribution of source terms,

$$\dot{\rho}_1 - \nabla\cdot[(D\Delta\tau)\nabla\dot{\rho}_1] = \dot{\rho}_0 \tag{13}$$

where $\Delta\tau$ is an artificial time step, and Neumann boundary conditions are imposed for the smooth source term field on all boundaries of the domain. Therefore, the integral values of the sharp and the smooth source fields remain the same, despite the smearing. The width of the smeared source term field is proportional to the square root of the product of the diffusion constant "D" and the artificial time step "$\Delta\tau$". It should be mentioned that the value of "D" must be adjusted to the mesh resolution such that the source term field is smeared over several cells.

Then, the source terms in all cells that do not contain pure liquid or vapor ($\alpha < 1 - \alpha_{cut}$ and $\alpha > \alpha_{cut}$, where α_{cut} may be set to 0.01) are artificially set to zero. This cropping step ensures that the source terms that are shifted into the pure vapor and liquid cells are only in the vicinity of the interface. The interface therefore is not subjected to any source terms and is only transported by the calculated velocity field. Therefore, the transport algorithm for the volume fraction field as well as the associated interface compression can work efficiently without any interference with the source term field. The remaining source term field is scaled individually on the liquid and the vapor side through the application of appropriate scaling coefficients. This scaling step ensures that the mass is globally conserved and that the evaporating or

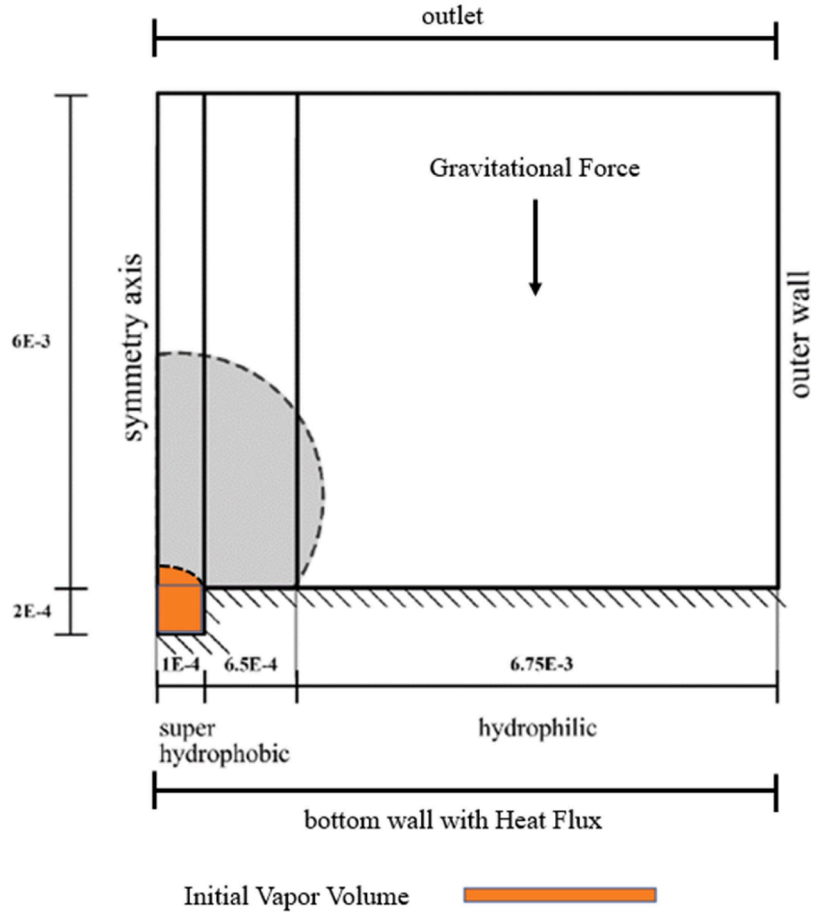

Fig. 12. Schematic of considered simulated phenomenon selected from [46] (dimensions in meters).

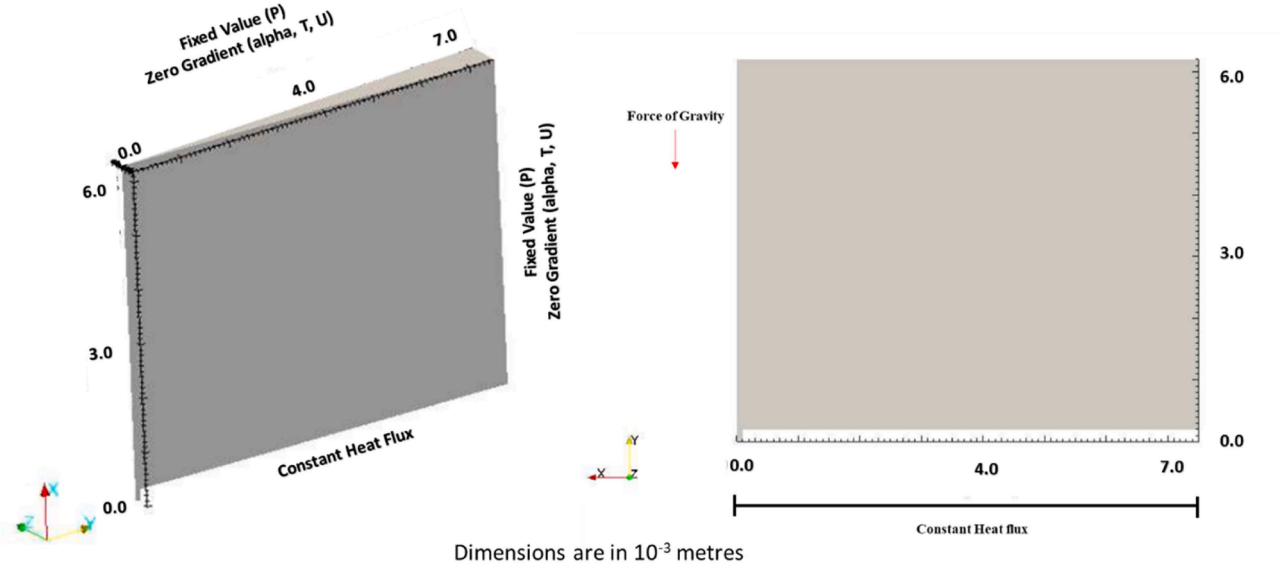

Fig. 13. Two-dimensional axisymmetric computational domain and boundary conditions (large scale case).

condensing mass flow corresponds globally to the net mass flow through the interface. The proposed scaling coefficients N_l and N_v are calculated by integrating the smooth source term field in each of the pure phases and comparing it to the net mass flow, $\dot{m}_{int}$(Eq. (12)), utilising the following equations:

$$N_l = \dot{m}_{\text{int}} \left[\int\int\int (\alpha - 1 + \alpha_{cut}) \dot{\rho}_1 dV \right]^{-1} \tag{14}$$

$$N_v = \dot{m}_{\text{int}} \left[\int\int\int (\alpha_{cut} - \alpha) \dot{\rho}_1 dV \right]^{-1} \tag{15}$$

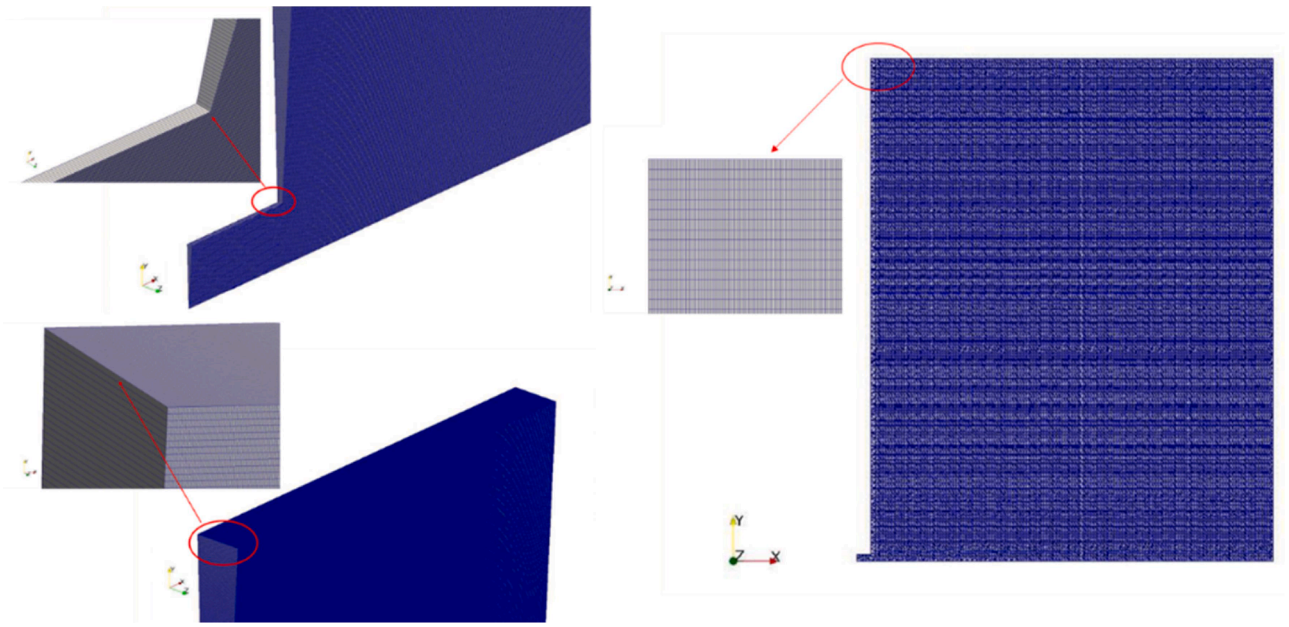

Fig. 14. Mesh of 2D axisymmetric geometry for water vapor and liquid.

Table 3
Material properties and initial conditions for the numerical simulations of water.

Property	Unit	Water	
		Liquid	Vapor
Density (ρ)	(kg/m^3)	957.45	0.62
Specific heat capacity (c_p)	(J/kg/K)	4220	2085
Thermal conductivity (k)	(W/m/K)	0.677	0.025
Dynamic viscosity (μ)	(Pa-s)	2.78e-4	1.23e-05
Heat of vaporization (h_{lv})	(J/kg)	2,253,100	
Surface tension (σ)	(N/m)	0.0587	
Saturation temperature (T_{sat})	(K)	374.39	
Pressure (P)	(bar)	1.0599	
Dynamic Contact Angle (θ)	(°)	Hydrophilic region: $\theta_a = 85.54$ ° $\theta_r = 34.37$ ° Super-hydrophobic region: $\theta_a = 160.88$ ° $\theta_r = 158.98$ °	
Heat Flux ($\dot{q}$)	(W/m^2)	200,000	

Finally, the final source term distribution is calculated using the above scaling factors in the following equation:

$$\dot{\rho} = N_v(\alpha_{cut} - \alpha)\dot{\rho}_1 - N_l(\alpha - 1 + \alpha_{cut})\dot{\rho}_1 \quad (16)$$

An example of the final source term distribution is depicted indicatively in Fig. 1 below.

The source term $\dot{h}$ of Eq. (3) is obtained from Eq. (17):

$$\dot{h} = \left[N_v(1-\alpha)C_{pv} - N_l\alpha C_{pl}\right]\dot{\rho}_1 T - \dot{\rho}h_{lv} \quad (17)$$

Where C_{pv} and C_{pl} represent the heat capacity of the vapor and the liquid phases, respectively. The first part of the source term corresponds to a correction source term that removes artefacts that emerge due to the structure or the mass source term in the proposed methodology. The second part of the source term represents the contribution of the enthalpy of evaporation or else the cooling associated with the latent heat of the phase change. Further details can be found in the work of Hardt and Wondra [41] that this methodology was originally proposed.

3. Application of the enhanced VOF based numerical simulation framework for lower spatial and temporal scales

As mentioned previously, as a first step for coupling two numerical methodologies that are applied at different spatial and temporal scales would be to explore their applicability limits at different scales. In this section, two different series of numerical simulations are performed to progressively explore the applicability of the previously presented enhanced VOF-based numerical framework for boiling heat transfer, in sub-micron scales. For the first series of simulations a widely used benchmark test case of a spherical bubble growth in a superheated liquid is selected. For the second series of simulations, various scenarios of singe bubble growth from superheated surfaces in saturated pool boiling conditions are considered, moving towards more realistic bubble growth scenarios.

3.1. Growth of a spherical bubble in a superheated liquid

The growth of a spherical vapor bubble within a superheated liquid domain constitutes a widely used test case for the validation of boiling models throughout the literature [41,45,63–65]. In general, the proposed growth follows two distinct stages. At the initial stage, the bubble growth is mainly controlled by the effects of surface tension and inertia. While in the second stage, the growth is mainly controlled only by the heat transfer rate from the superheated liquid to the liquid-vapor interface. During this final stage, it can be assumed that the bulk vapor and the liquid-vapor interface are at saturation temperature. The bubble size at this stage is quite large in order to safely neglect the vapor saturation temperature rise due to the pressure jump across the interface [63]. More details regarding the simulated phenomenon are described in detail in the work of Plesset and Zwick [65]. An analytical solution for this situation has been derived by Scriven [66]. According to this analytical solution, the bubble radius as a function of time is given by the following equation:

$$R(t) = 2\beta\sqrt{Dt} \quad (18)$$

where β is a growth constant, the details of which can be found in the work of Scriven [66], and D is the thermal diffusivity of the liquid. The proposed analytical solution is the one usually adopted in previous VOF based boiling model validations [41,45,63–65], since the targeted

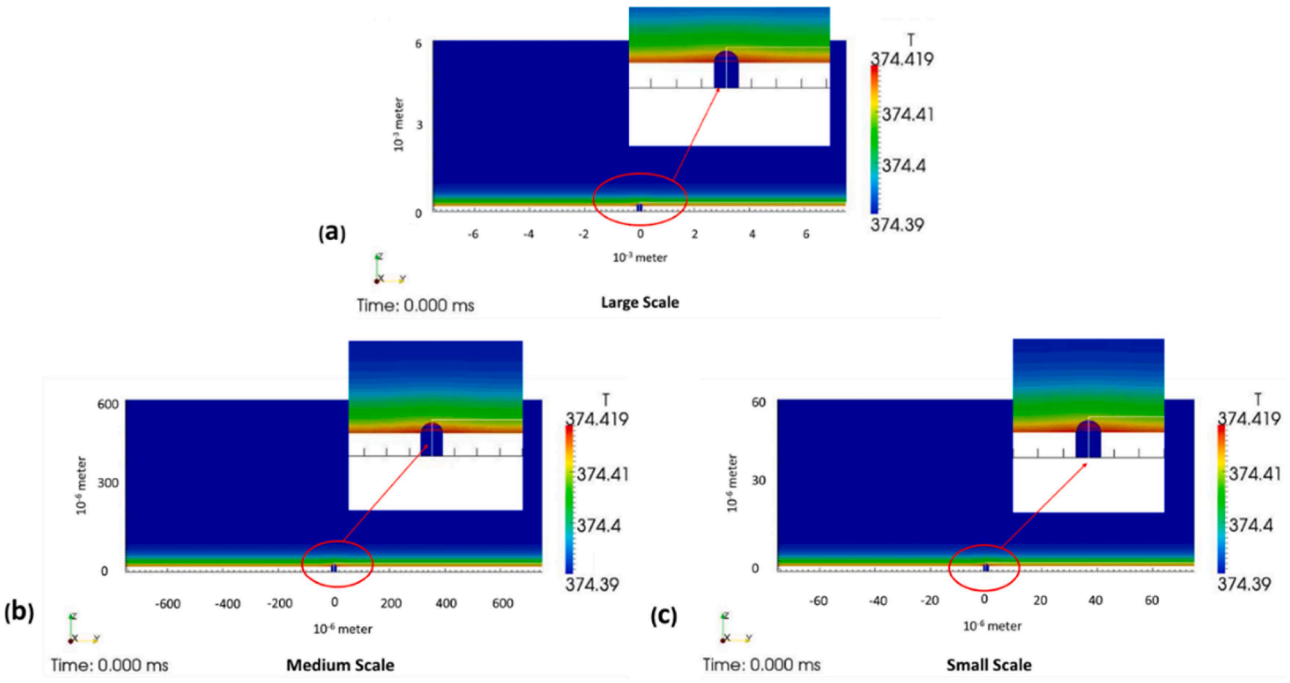

Fig. 15. Initial temperature profile of the domain with water-vapor bubble for (a) large scale, (b) medium scale (1/10), and (c) small scale (1/100).

simulations were for relatively large bubbles that fall within the second stage of bubble growth.

However, for the purposes of the present investigation, that explores progressively smaller bubbles potentially falling into the first stage of bubble growth, it was deemed appropriate to additionally compare the present VOF model predictions with another analytical solution provided by Mikic et al. [67], that accounts for both stages of bubble growth (i.e. both the inertia-controlled growth as well the diffusion heat-transfer controlled growth stages). The general bubble growth relation obtained from Mikic et al., is described by Eqs. (19) and (20).

$$R^{+} = \frac{2}{3}\left[(t^{+}+1)^{\frac{3}{2}} - (t^{+})^{\frac{3}{2}} - 1\right] \tag{19}$$

$$t^{+} = \frac{A^{2}t}{B^{2}} \tag{20}$$

Here, R^{+} and t^{+} are non-dimensional radius and time. The formulations for A and B are given by Eqs. (21) and (22), respectively. In Eq. (22), (Ja) represents the Jacob number, which is calculated by Eq. (23), while c_{pl} and h_{fg} represent the specific heat of the liquid phase and the specific enthalpy of vaporization, respectively.

$$A = \left(\frac{2}{3}\cdot\frac{h_{fg}\cdot\rho_{v}\cdot\Delta T}{\rho_{l}\cdot T_{sat}}\right)^{\frac{1}{2}} \tag{21}$$

$$B = \left(\frac{12}{\pi}\cdot D\right)^{\frac{1}{2}}\cdot Ja \tag{22}$$

$$Ja = \frac{\Delta T\cdot c_{pl}\cdot\rho_{l}}{h_{fg}\cdot\rho_{v}} \tag{23}$$

To perform the numerical analysis an initial thermal boundary is required to be patched on the outer surface of the bubble in the liquid region. As in previous similar investigations [45,63,65], a parabolic fit is used to mimic the growth of thermal boundary layer as shown in Fig. 2. Furthermore, the coefficients of parabola are evaluated based on the Eqs. (24), (25) and (26).

$$T(r = R_{0}) = T_{sat} \tag{24}$$

$$T(r = R_{0}+\delta_{T}) = T_{\infty} \tag{25}$$

$$\frac{\partial T}{\partial r}(r = R_{0}+\delta_{T}) = 0 \tag{26}$$

This analytical solution permits the calculation of the initial conditions for the numerical simulations (initial temperature profile at the bubble interface and initial bubble radius) in order to validate the numerical predictions. The geometric characteristics and the initial conditions of the considered physical problem are illustrated schematically in Fig. 3.

Three different two-dimensional axisymmetric simulations were performed for three different working fluids, water, and FC-72 liquid at equilibrium with their corresponding vapor phases (saturation point), at a pressure value of 1013 mbar, as well as R134a liquid at equilibrium with its vapor phase at a pressure value of 840 mbar. The first simulation for each working fluid case corresponds to a typical initial bubble size from the heat-transfer controlled stage of bubble growth. The remaining two simulations for each case correspond to a progressive reduction of the initial bubble size by a factor of 10 and 100, respectively. For this purpose, the overall typical scale computational domain is scaled down by the proposed factors. For the typical scale domains, uniform hexahedral grids of a 0.5 μm cell dimension were used for all three working fluid scenarios. Previous mesh independency studies with the same numerical simulation framework [37,53] indicated that accurate interface dynamics and evaporation rates can be predicted with a cell size of at least 2 μm. In the present simulations, an even finer cell size of 0.5 μm is necessary to resolve the thin thermal boundary layer surrounding the bubble interface, during the investigated phenomenon. The computational domain and grid that was constructed as well as the applied boundary conditions for the typical scale runs are depicted in Fig. 4. The initial conditions for the water liquid/vapor case are illustrated indicatively in Fig. 5, while the material properties and the initial conditions for all fluid cases are summarized in Table 1.

In Figs. 6 to 8, the reconstructed three-dimensional spatial and temporal evolution of the numerically predicted bubble growth is illustrated indicatively for the water liquid/vapor case, for each of the considered scales. Here, alpha1 signifies the volume fraction (α) of the liquid phase.

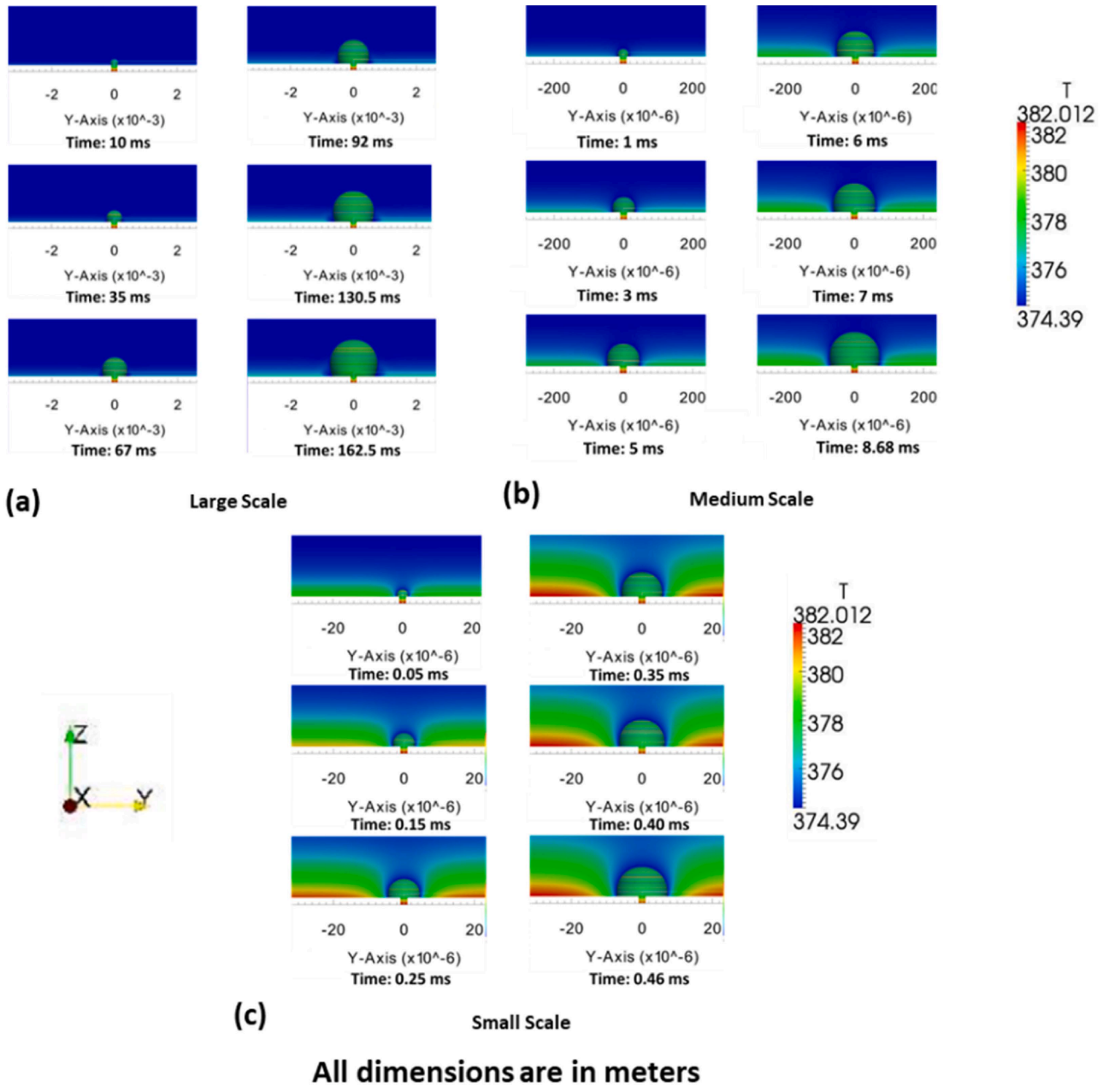

Fig. 16. Qualitative result and temperature profile of uniform wettability for (a) large scale, (b) medium scale (1/10), and (c) small scale (1/100).

From a qualitative point of view, as it is expected for all three cases, due to the temperature difference between the superheated liquid domain with the saturated vapor inside the bubble, evaporation occurs at the interface and the bubble radius grows with time.

For a more quantitative point of view and in order to investigate the accuracy of the overall predictions for all three considered working fluids and all three scales, Figs. 9 to 11, contain a quantitative comparison of the VOF model predictions with both of the previously described analytical solutions. For this purpose, the predicted dimensionless bubble radius (R') in each case is plotted against a dimensionless time (τ). The resulting plots for Water, R134a and FC72 are illustrated in Figs. 9, 10 and 11, respectively. The analytical solutions by Scriven [66] and by Mikic et al. [67] in these plots, are calculated for the same initial and operating conditions as the corresponding numerical runs. The initial radius (R) of the bubbles is taken as 100 μm for the large-scale case and 10 μm and 1 μm for the medium and small-scale cases, respectively. The dimensionless bubble radius (R') corresponds to the dimensional values of bubble radius (R) normalized by a characteristic length (L_0) which is calculated as the square root of the ratio of the surface-tension co-efficient to the product of the acceleration due to gravity and the density difference between the liquid and vapor phases, shown in Eq. (27). The dimensionless time (τ) corresponds to the ratio of the actual time (t) to a characteristic time (t_0) that is calculated as the square root of the ratio of the characteristic length (L_0) to the acceleration due to gravity (g), shown in Eq. (28).

$$L_0 = \sqrt{\sigma/((\rho_l - \rho_v)g)} \tag{27}$$

$$t_0 = \sqrt{L_0/g} \tag{28}$$

$$R' = R/L_0 \tag{29}$$

$$\tau = t/t_0 \tag{30}$$

As it can be observed, for the case of water (Fig. 9) the considered

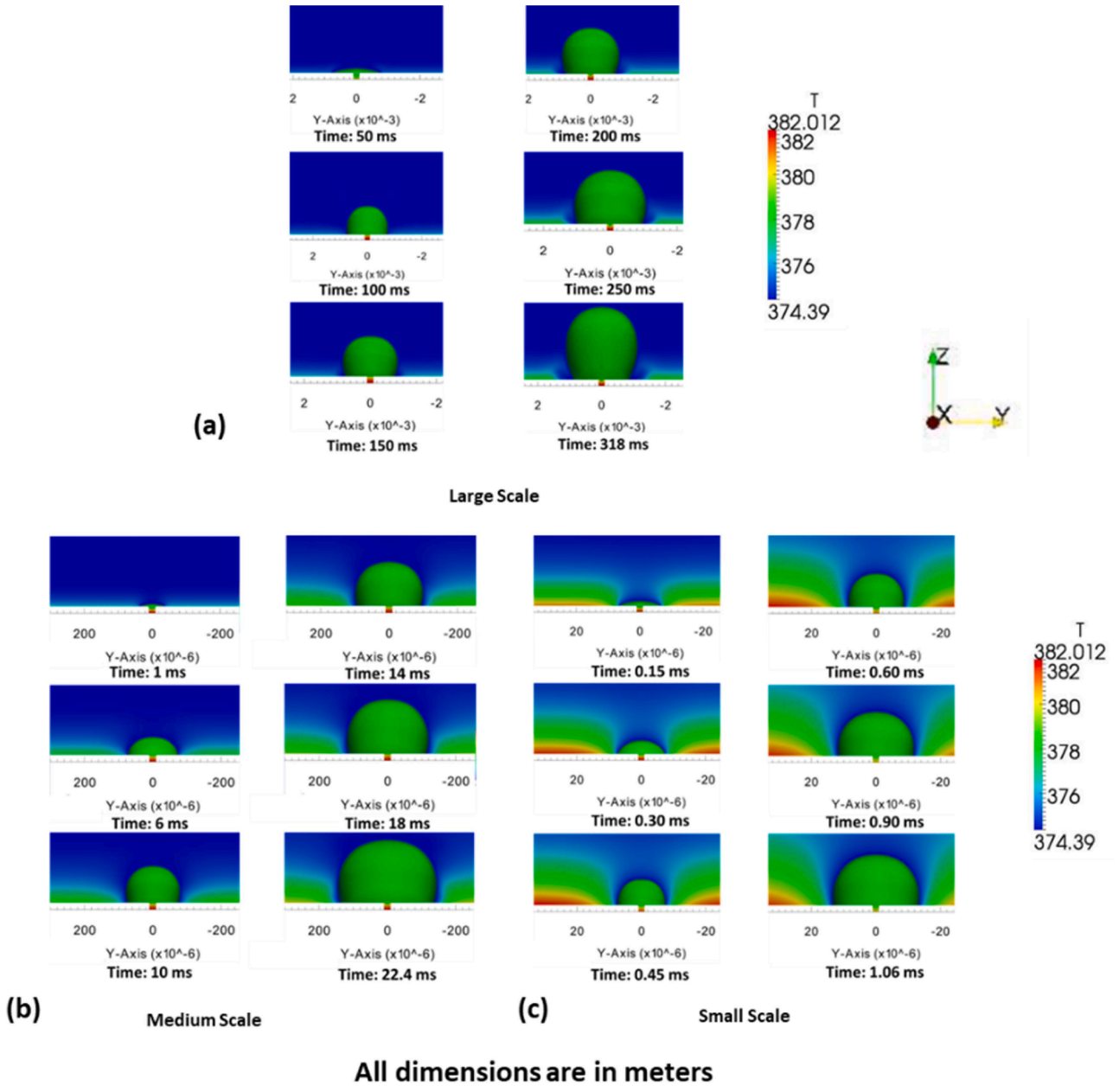

Fig. 17. Qualitative result and temperature profile of variable wettability for (a) large scale, (b) medium scale (1/10), and (c) small scale (1/100).

VOF-based numerical simulation framework predictions are in close agreement with both the analytical solutions by Scriven [66] and Mikic et al. [67] only for the large-scale case (blue color points). For the medium and small scales, the VOF model prediction are in closest agreement with the analytical solution of Mikic et al. (black dashed line) while deviating progressively from the analytical solution of Scriven (grey line). The reason for this observation is the fact that the analytical model provided by Scriven is more suited for diffusion heat transfer controlled growth rates, that lies in the macro-scale region. Furthermore, the surface-tension coefficient is higher for the case of water than the other refrigerants. The formulation provided by Mikic et al. accounts for the effect of surface-tension in the bubble growth, that lies in the lower-scale region, while the solution of Scriven et al., only accounts for the second stage of the bubble evolution due to heat transfer. Therefore, the numerically predicted curves of water for lower scales show higher deviation from the Scriven et al. solution and move more towards the Mikic's solution compared to the other refrigerants. A similar trend is observed for the other two considered working fluids (Figs. 10 and 11) in which cases however, the deviation of the VOF model predictions from the analytical solution by Scriven is more evident at the smallest of the considered cases. Since the VOF model predictions for all three scales and all three working fluids are in close agreement with the generalized analytical solution of bubble growth by Mikic et al. that considers both the inertia controlled growth stage as well the diffusion heat transfer controlled growth stage of the bubbles it can be concluded that the proposed VOF-based numerical simulation framework can be safely applied for significantly lower spatial and temporal scales, up to at least two orders of magnitude than the typical application scales of VOF-based methodologies in the literature that usually consider the growth of vapor bubbles in domains that span from hundreds of μm up to hundreds of mm. The quantitative deviation range is shown in Table 2.

For the lower scale cases considered, initial embryo bubbles of 1 μm in radius and computational domain of a characteristic dimension of 8 μm are utilised. Such scales are approaching the upper application limit for the Fluctuating Diffuse Interface (FDI) mesoscale approach recently presented by Gallo et al. [29]. Therefore, the outcome of the present

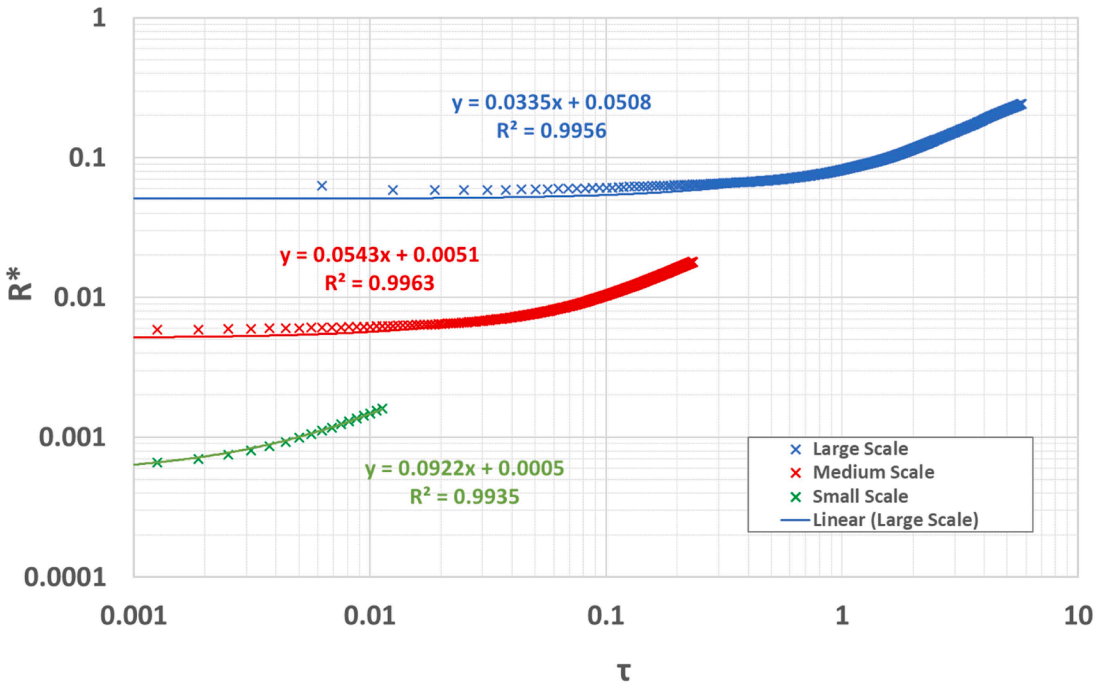

Fig. 18. Plot of non-dimensional radius vs non-dimensional time for the case of uniform wettability with the scenarios of large scale, medium scale (1/10), and small scale (1/100).

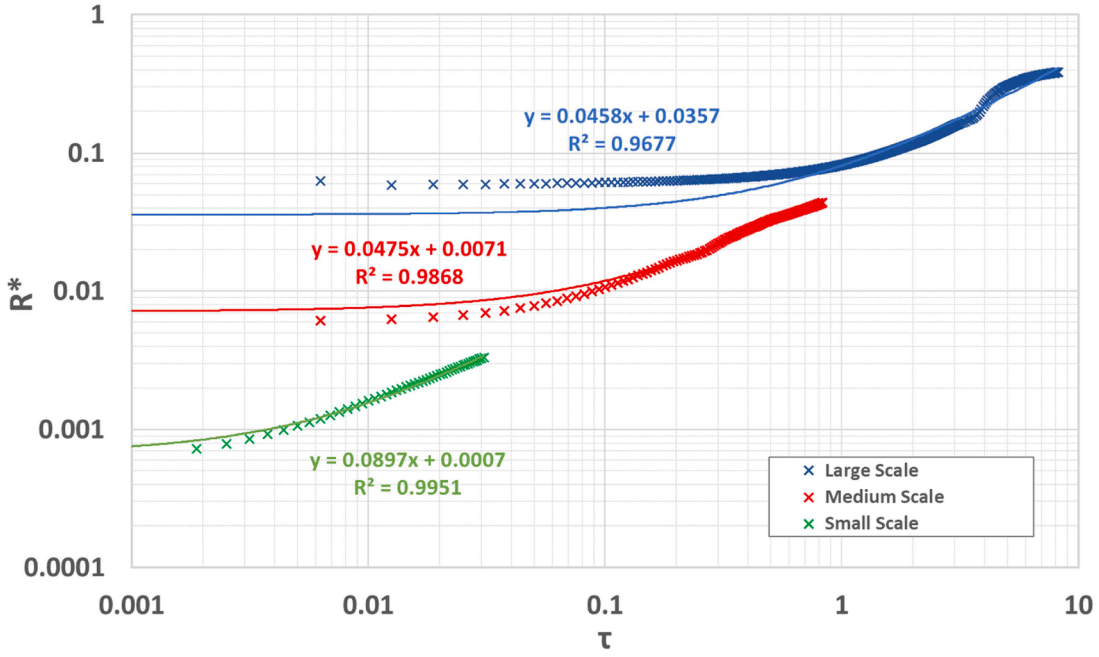

Fig. 19. Plot of non-dimensional radius vs non-dimensional time for the case of variable wettability with the scenarios of large scale, medium scale (1/10), and small scale (1/100).

investigation that illustrates for the first time that the proposed VOF method can accurately predict the bubble growth characteristics at such small scales, paves the way for the future indirect or even direct coupling of these two numerical modelling approaches into a multiscale numerical simulation framework for boiling heat transfer. Such a future hybrid framework could therefore physically account and predict all relevant scales of bubble generation and development, i.e. from bubble nucleation up to bubble growth, detachment and bubble to bubble interaction leading to a comprehensive, complete, and accurate prediction of two-phase boiling regimes.

3.2. Single bubble growth from superheated plates of uniform and variable wettability in saturated pool boiling conditions

The utilized VOF-based numerical simulation framework of the present investigation, has been previously validated and successfully applied for various cases of pool and flow boiling [37,67] that represent more realistic scenarios of pool boiling and flow boiling heat transfer where vapor bubbles grow and detach from superheated plates within stagnant or flowing liquid domains. The same model has also been successfully applied for various cases of adiabatic as well as diabatic

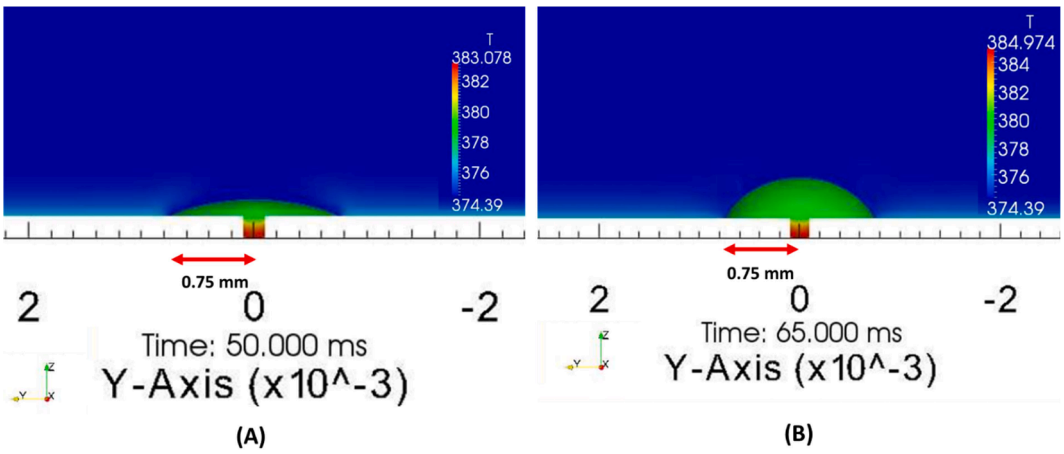

Fig. 20. Size of the vapor bubble at (a) 5τ and (b) 6.5τ. The red double arrow shows the extend of the hydrophobic region.

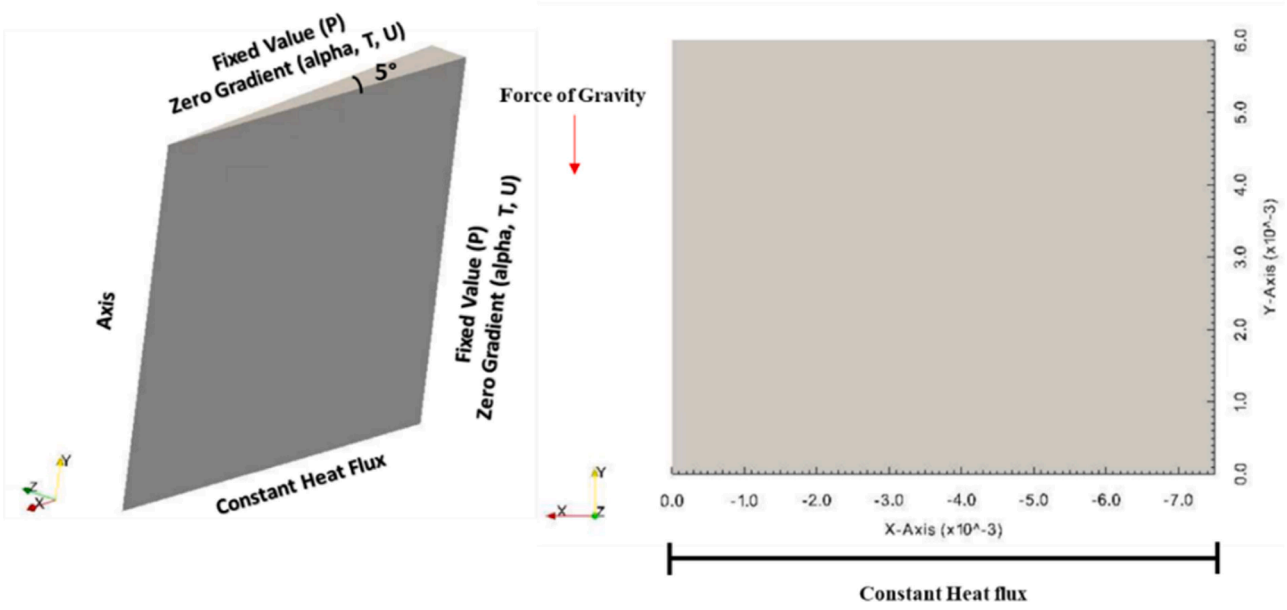

Fig. 21. 2D axisymmetric domain of ethanol liquid and vapor for normal (large) scale.

bubble and droplet dynamics [36,68,69] However, in all these previous successful applications of the model the considered computational domains span from hundreds of μm up to hundreds of mm. It was therefore deemed appropriate to expand the purposes of the present investigation and further test the applicability proposed VOF model at progressively lower spatial and temporal scales not only for theoretical benchmarks but also for the case of more realistic scenarios of heterogeneous boiling. Therefore, in this section cases of single bubble growth from superheated plates, under saturated pool boiling conditions for both uniform and variable wettability characteristics are considered.

The base case for the proposed numerical investigation has been selected from a previous investigation where the validity of the utilized VOF based numerical simulation framework has been checked against an experimental run of a single water bubble growing and detaching from a superheated bi-phillic surface [70], consisting of a hydrophilic stainless-steel foil with a circular superhydrophobic spot in the middle. Since the investigated phenomenon presents an axial symmetry, to save computational time, a 5° 3D wedge domain with a symmetry axis is constructed, in order to perform 2D-Axisymmetric simulations. The considered physical phenomenon and the constructed computational domain for the base case are depicted in Figs. 12 and 13, respectively.

On the base of the domain, near the bubble center, an artificial cavity was placed. When setting the initial conditions, the purpose of the cavity will be to hold some vapor from which a successive bubble will grow after the pinch-off and detachment of the first bubble embryo that is patched within and on top of this cavity. However, it should be mentioned that the present investigation is focused only in the first bubble cycle. The domain base must also be divided accordingly in superhydrophobic and hydrophilic regions. A different boundary condition is applied to each wall, assigning the corresponding advancing, and receding contact angles as resulted from sessile drop measurements [70]. A constant heat flux is also applied along the bottom wall boundary, in both regions. The fluid domain consists of bottom wall, side wall, outlet, and axis of symmetry. Details regarding the applied boundary conditions are included in Fig. 13. This base case computational domain after meshing and setting up all boundary and initial conditions is then scaled down by a factor of 10 as well as by a factor of 100 to progressively explore the predictions and hence the applicability of the proposed VOF method at sub-micron scales, in analogy to the previous section of the present investigation. The physical dimensions of the computational domain for the large-scale simulation are 6.2 mm along the y-axis direction and 7.5 mm along the x-axis. The length of

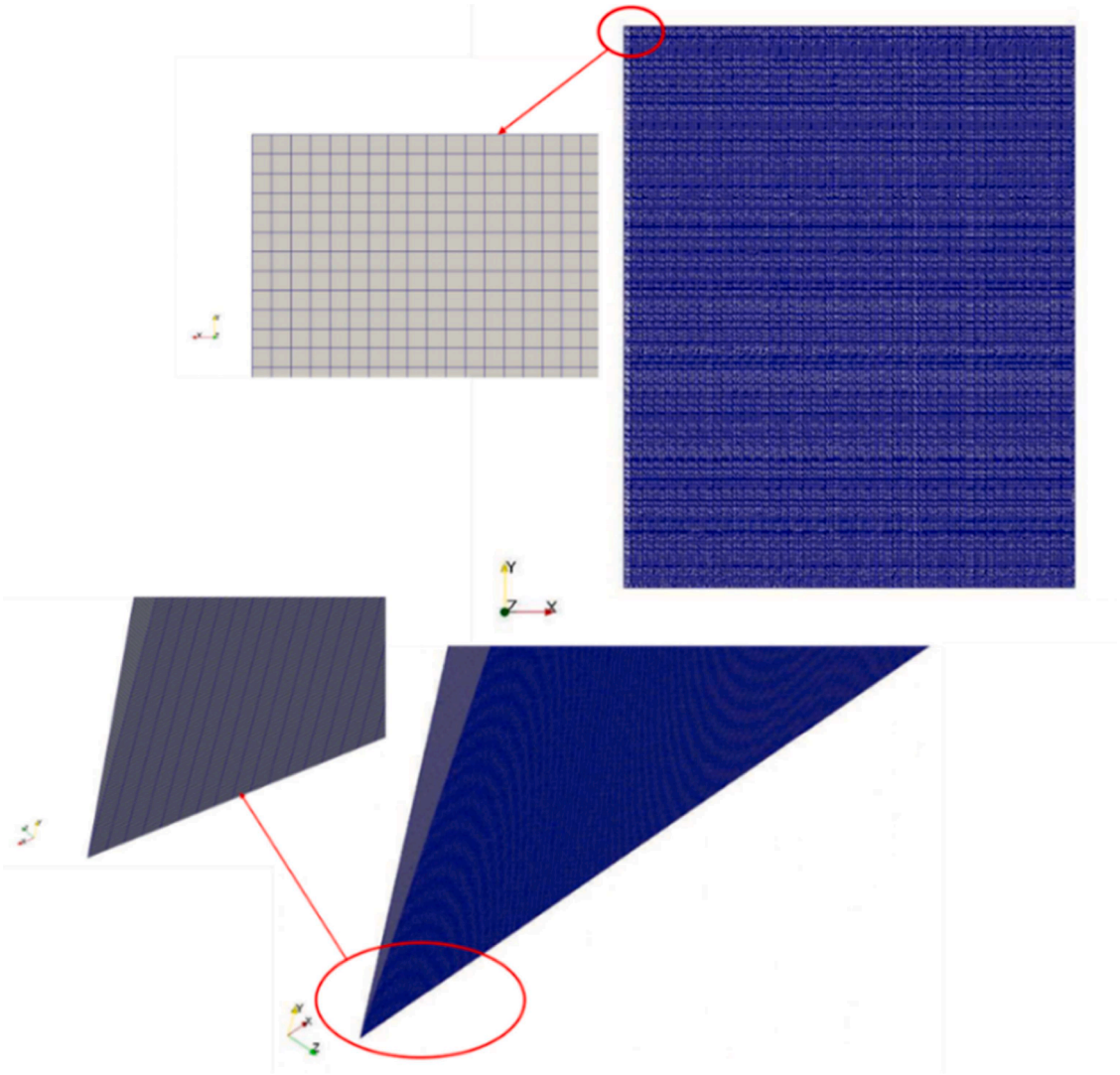

Fig. 22. Mesh of 2D axisymmetric geometry for ethanol vapor and liquid.

hydrophobic surface is 0.75 mm and the length of hydrophilic surface is 6.75 mm respectively. The cavity is 0.2 mm long and 0.1 mm wide. For the medium and small-scale cases, the corresponding values are reduced to 1/10th and 1/100th, respectively.

Hexahedral mesh elements are dominant in the domain, while prismatic cells are present near the axis of symmetry. For the large-scale domain, the minimum element size used for the normal scale is 2 μm. The mesh density is higher near the region of the cavity. The regions near the side wall and the top boundary contain larger cells due to the applied growth factor in the directions away from the cavity. The corresponding minimum element sizes for the medium and small-scale cases are 0.2 μm and 0.02 μm, respectively. The computational mesh for the large scale is shown in Fig. 14. For all three scales, the total mesh elements are 2.1 million, minimum orthogonal quality is 1, and maximum aspect ratio is 5, indicating high quality meshes. It must be noted here that the minimum cell size of 2 μm that was used for the base case is a result of previous mesh independency studies with the proposed VOF method [36,68–70].

The liquid and vapor properties that were used for the simulations are summarized in Table 3 and are taken from Pontes et al. [71]. The analysis is started for single-phase using water-liquid. In this scenario a constant heat flux is applied as a boundary condition on the bottom wall. The analysis is run for 0.23 s to obtain a well-developed initial thermal boundary layer. The results of the last time step of the single-phase simulation with the initially developed thermal boundary layer are then used as an initial condition for the two-phase analysis. Water-vapour is then patched within the cavity and on top of the cavity in the form of a 5-degree wedge of a hemispherical vapour cap of radius of 100 μm with a temperature equal to the saturation temperature, as shown in Fig. 15. From the images it is evident that the thermal boundary layer is well established and fully encapsulates the initial water-vapour embryo bubble. At this point it has to be mentioned that the same process is repeated also for cases where the entire bottom boundary is of uniform hydrophilic wettability.

The qualitative results of the temporal and spatial evoulution of the liquid/vapour interface with superimposed temperature profiles at a central vertical section, for the large, medium and small scale domains and for uniform hydrophillic as well as biphillic cases are shown in Figs. 16 and 17, respectivelly.

As it can be observed from Figs. 16 and 17, the thickness of thermal boundary layer is higher in comparison to the bubble height as the scale of the bubble minimizes, since for all three of the considered scales the applied heat flux value remains constant and the spatial and temporal scales are progressively lower. Hence, despite the same relative analogies at the initial time step, as the absolute scale of the domain reduces the initial thermal boundary layer grows faster in relation to the growth of the initial bubble embryo. This leads to a situation that as the scale reduces, a progressively higher percentage of the liquid/vapor interface

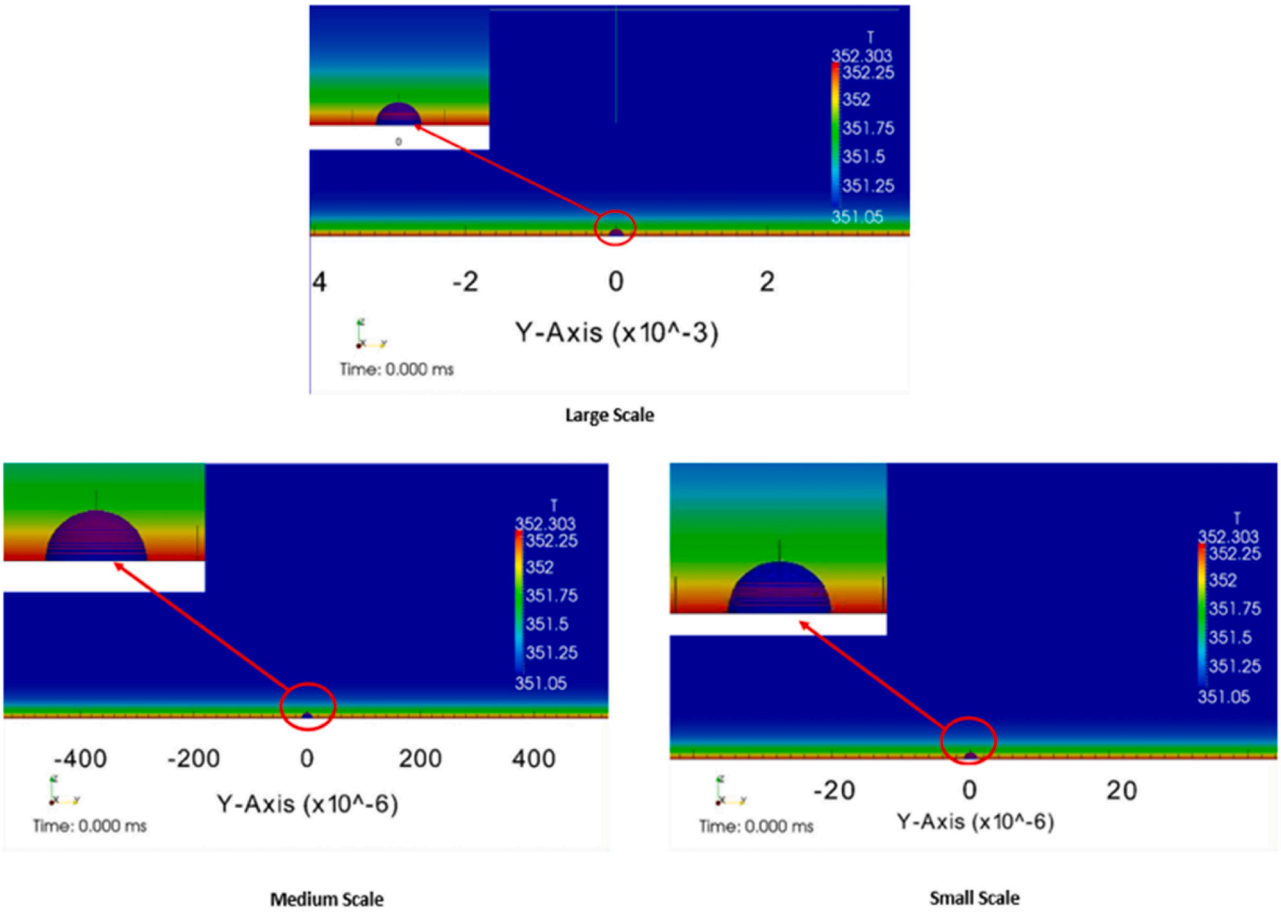

Fig. 23. Initial temperature profile of the domain with ethanol-vapor bubble for all three considered scales.

Table 4
Material properties and initial conditions for the numerical simulations of ethanol.

Property	Unit	Ethanol	
		Liquid	Vapor
Density (ρ)	(kg/m^3)	736.78	1.6269
Specific heat capacity (c_p)	(J/kg.K)	3181.8	1804.4
Thermal conductivity (k)	(W/m.K)	0.153	0.022
Dynamic viscosity (μ)	(Pa.s)	4.43e-04	1.04e-05
Heat of vaporization (h_{lv})	(J/kg)	850,530	
Surface tension (σ)	(N/m)	0.0153	
Saturation temperature (T_{sat})	(K)	351.05	
Pressure (P)	(bar)	0.99	
Dynamic Contact Angle (θ)	(°)	Hydrophilic region: $\theta_a = 19^\circ$ $\theta_r = 18^\circ$	
Heat Flux ($\dot{q}$)	(W/m^2)	100,000	

is in contact with a superheated liquid domain, leading to relatively steeper growth rates.

This becomes even more evident in the quantitative comparison of Figs. 18 and 19. In these figures, logarithmic plots of dimensionless radius versus dimensionless time are depicted. For this purpose, the non-dimensional equivalent radius in each case versus the non-dimensional time are plotted for all three considered scales for each of the two wettability scenarios, respectively. The equivalent radius of the bubble is calculated considering a sphere with the same volume as the vapor volume within the computational domain at any time instance, after a 3D reconstruction of the axisymmetric numerical predictions. The corresponding parameters are normalized with the same characteristic length definition as mentioned in Eq. (27), and the same characteristic time definition shown in Eq. (28) as in the previous section of the investigation (Section 3.1). Best fit lines are also added and their resulting equations and R^2 values are indicated in each case. The high R^2 values, indicate that the resulting equations fit the numerically predicted data very well for each case. For each dataset, the resulting best-fit line equation is of the following form,

$$\log(R^*) = m \times \log(\tau) + b \tag{31}$$

where m is the slope, and b is the y-intercept. Due to the fact that these curves are presented in a logarithmic scale, the slope m in effect represents the power-law exponent characterizing the bubble growth rate.

Comparing the bubble growth versus time between the uniform and variable wettability cases it can be observed that the curves for the medium and small cases show similar trends, while for the large scales and in the case of the variable wettability surface a non-uniform growth rate is observed. The change in the growth rate of the bubble is after $\tau = 4$. At this time instance, the triple contact line reaches at the boundary between the hydrophilic and super-hydrophobic regions. In more detail the bubble grows initially sliding along the superhydrophobic region and when it reaches at $\tau = 4$ at the bi-phillic boundary pinning occurs and it continues to grow mainly in the vertical direction. The proposed phenomenon is illustrated in Fig. 20.

Comparing now the different scales for both the variable (Fig. 18) and uniform (Fig. 19) wettability scenarios the large-scale case has the lowest slope, which progressively increases for the medium scale and the small-scale cases, respectively. This suggests that the generated bubble grow fastest relative to the characteristic scales at the small scale, and slowest at the large scale. The differences in slopes with respect to the characteristic scales are quite significant, for both the variable as well as

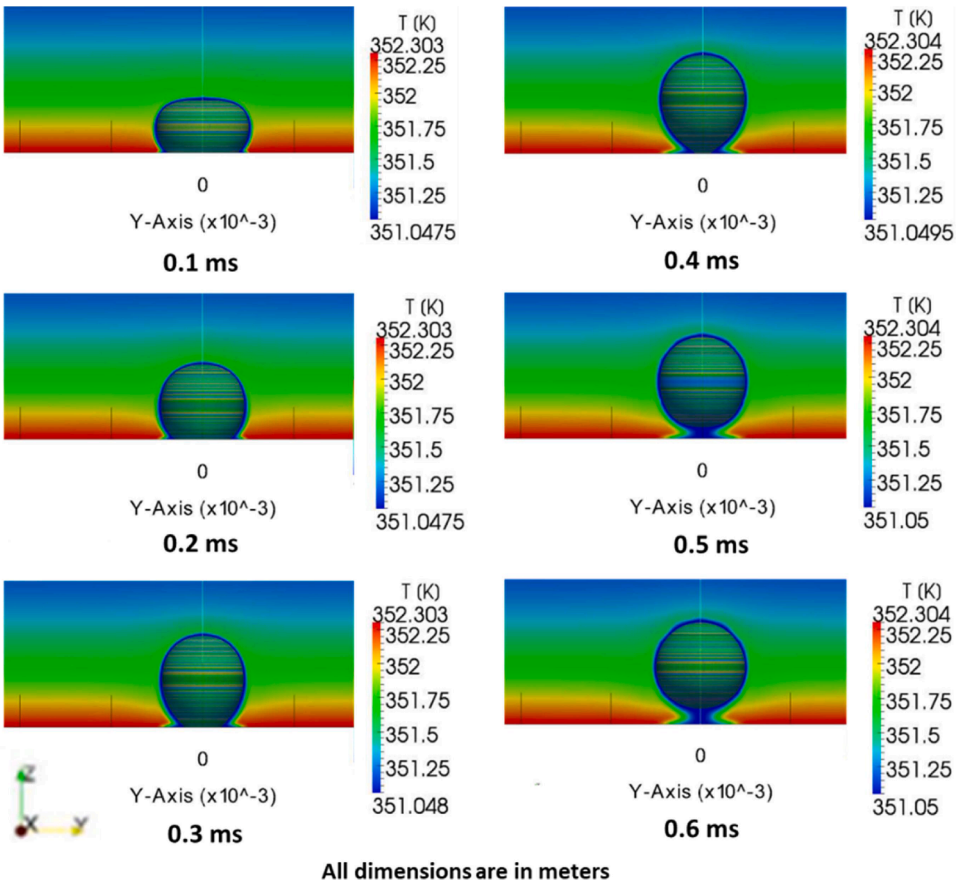

Fig. 24. Ethanol vapor bubble qualitative result and temperature profile of uniform wettability for large scale scenario.

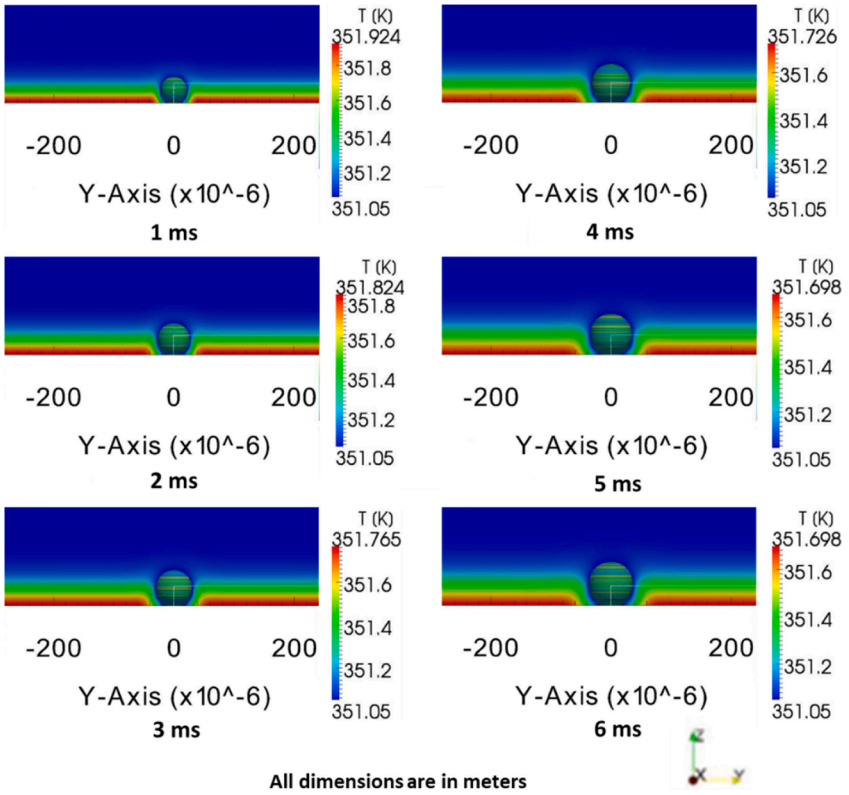

Fig. 25. Ethanol vapor bubble qualitative result and temperature profile of uniform wettability for medium scale (1/10) scenario.

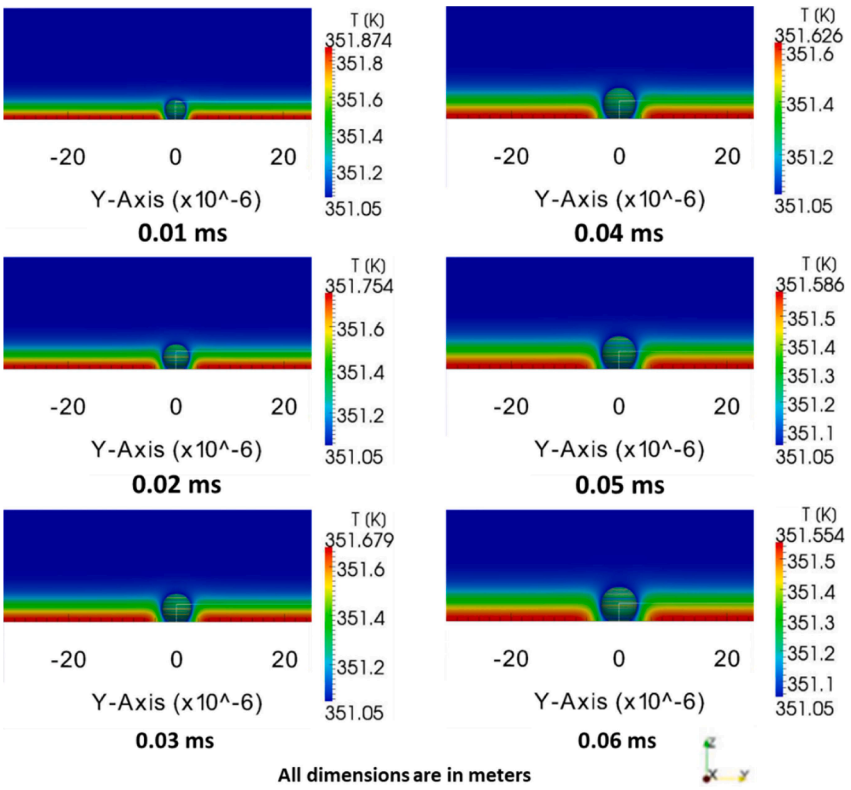

Fig. 26. Ethanol vapor bubble qualitative result and temperature profile of uniform wettability for small scale (1/100) scenario.

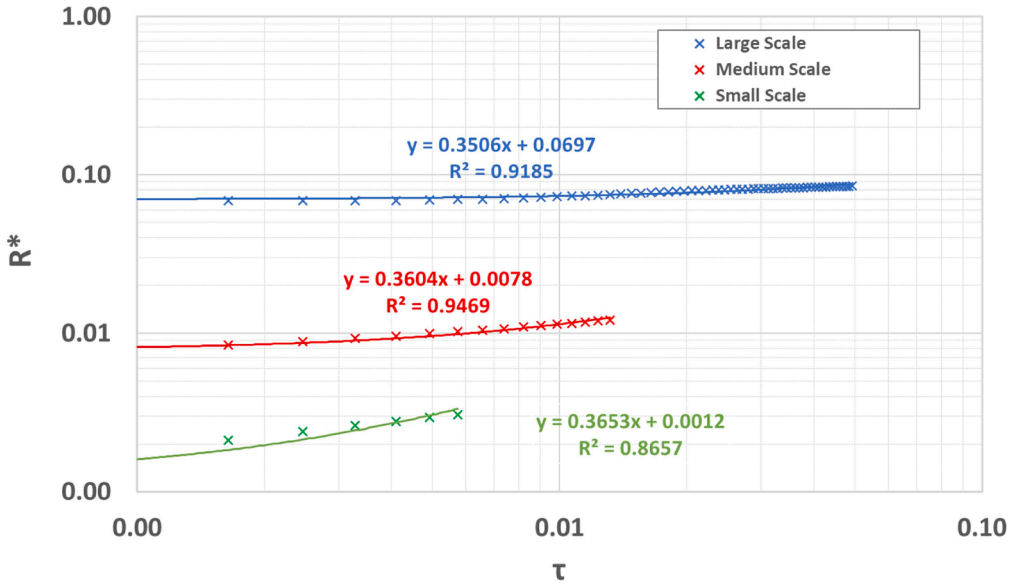

Fig. 27. Plot of dimensionless equivalent radius vs dimensionless time for the cases of uniform wettability of Ethanol with the scenarios of large scale, medium scale (1/10), and small scale (1/100).

the uniform wettability scenarios. The y-intercepts also increase from large to small scale, but their differences are relatively small compared to the changes in R* over the plotted range. In summary, from the resulting log-log plots it is demonstrated that the bubble growth follows a power-law behavior with different exponents across the three scales investigated. The growth rates increase as the scale becomes smaller, indicating a scale-dependent behavior in the bubble growth dynamics under these conditions. As also discussed previously, this observation can be attributed to the fact that as the scale of the investigated phenomenon changes the initial thermal boundary layer grows differently in relation to the growth of the initial bubble embryo, leading to different percentage of the liquid/vapor interface being in direct contact with a superheated liquid domain which results to different evaporation rates. Moreover, at different scales the relative importance between the forces that act on the bubble is quite different.

From the overall analysis and discussion on the results in this section it is evident that the utilized VOF-based numerical simulation framework gives reasonable predictions as the spatial and temporal scales of

the simulation are progressively reduced. Unfortunately, to the best of the authors' knowledge there are not any experimental measurements available in the literature at such small temporal scales and this is the reason that the discussion is focused on a physical interpretation of the observed bubble growth characteristics.

3.3. Growth of an ethanol-vapor bubble on surfaces with uniform wettability with constant heat supply

In this section the proposed VOF-based solver is further applied to study the growth of an ethanol-vapor bubble from a uniformly heated plate with uniform wettability characteristics. The wettability characteristics as well as the thermophysical properties of ethanol are taken from Andredaki et.al [34].

This analysis was also conducted in order to check the applicability of the VOF solver in lower scales as in the previous sections but considering a working fluid with lower surface tension and heat of vaporization than water in order to simulate faster and study the case of a complete bubble growth up to the point that the bubble detaches from the heated surface.

The considered computational domain and the applied boundary conditions for the large-scale case are depicted in Fig. 21.

The size of the domain is 6 mm × 7.5 mm, however in this case in order to reduce complexity the no cavity has been removed from bottom wall. Like in the previous section (Section 3.2), lower scales are also considered by reducing the large scale to 1/10th (medium scale) and 1/100th (small scale). The domain shape is again axisymmetric, with a 5° wedge. The vertical wall adjacent to the bubble is a symmetry axis, in order to perform 2D-Axisymmetric simulations. The boundary conditions applied to the bottom wall is a constant heat flux. Hexahedral mesh elements are dominant in the domain, while prismatic cells are present near the axis of symmetry. The minimum element size used for the normal scale is 2 μm. Mesh details are shown indicatively in Fig. 22, for the large-scale case. The mesh density is higher near the region of the initial bubble embryo. The regions near the vertical and top boundaries contain larger cells due to the imposed growth factor away from the initial bubble embryo region (bottom left corner of the axisymmetric computational domain).

The analysis is initiated using a single-phase simulation with liquid ethanol. As mentioned previously, a constant heat flux is applied as a boundary condition at the bottom wall. The analysis is run for 0.5 s to obtain a well-developed thermal boundary layer. The result of the last time step of the single-phase simulation with the initially developed thermal boundary layer is used as an initial input for the two-phase analysis. Furthermore, an ethanol-vapor embryo is patched having a radius of 100e-6 meter and a temperature value of 351.05 K (saturation temperature), as shown in Fig. 23. The utilized material properties, initial and operating conditions are summarized in Table 4. The qualitative results of the bubble growth with a superimposed temperature profile in a central vertical section are depicted in Fig. 24, for the large-scale case. The bubble immediately starts to evaporate with the contact line initially advancing and then receding leading to the final detachment of the bubble from the smooth hydrophilic surface at $t = 0.5$ msec. The bubble generation takes place in two stages: growth and detachment. In the initial stages of growth, the bubble enlarges in size. The surface tension is the driving force during this stage and the bubble remains attached to the wall. At a certain point as the bubble grows the buoyancy force becomes greater than the surface tension force and the bubble starts to recede and eventually detaches from the bottom wall. The corresponding results for the medium and small-scale cases are illustrated in Figs. 25 and 26, respectively. For the smaller scales, up to the simulated flow times in each case, the bubbles grow with an advancing contact line. However, comparing the evolution of the bubbles between the three considered scales it can be observed that as the scale is progressively reduced the relative growth rate of the bubble with respect to the growth of the initial thermal boundary layer is progressively increasing, while the bubble remains attached at the heated wall. This is because at lower scales the relative importance of the buoyancy force with respect to the surface tension force is significantly reducing.

For a more quantitative comparison of the bubble growth rates the logarithmic plot of the dimensionless equivalent bubble radius with respect to the dimensionless time is illustrated in Fig. 27, for the large-scale, medium-scale, and small-scale cases. Best fit lines with their resulting equations and R^2 values are also shown in each case. As in the previous section the relatively high R^2 values, indicate that the resulting equations fit the numerical data very well for each case. Also, for each dataset, the resulting best-fit line equation is of the same form as the one previously described in Eq. (24).

However, comparing the slopes of the best-fit lines, it is observed that they are very similar across all three scales, ranging from 0.3506 to 0.3653, increasing slightly with the decrease of the scale almost within ~4% of each other. This suggests that the effect of the scale change in the dimensionless bubble growth rate is quite small for the ethanol scenario in comparison to the water scenarios of the previous section. This might be attributes to the relatively lower values of surface tension and heat of vaporization as well as to the significantly lower contact angles for the ethanol case.

From all the above, also in this section, it can be concluded that the utilized VOF-based numerical simulation framework predictions are reasonable and can indeed have a physical interpretation for the hypothetical ethanol bubble growth scenarios at three different scales that are considered.

4. Conclusion

In the present work, an enhanced VOF-based numerical simulation framework that accounts for spurious currents reduction, enhanced dynamic contact angle modelling for wettability effects, and phase change due to boiling and condensation that has been previously developed in OpenFOAM, has been further employed to explore its applicability at lower spatial and temporal scales. The main aim for the proposed investigation was to explore the boundaries of the proposed VOF method to scales where mesoscale numerical modelling approaches and particularly the Fluctuating Diffuse Interface (FDI) method are usually applied, in order to pave the way for the future easier coupling of these two numerical approaches into a hybrid multi-scale numerical framework for boiling flows.

For this purpose, a first step the growth of a spherical bubble in a superheated liquid domain was considered for three different working fluids (water, R134a, FC72) and the VOF model predictions were compared with two analytical solutions for three progressively lower scales, spanning from the typical macro-scales up to sub-micron scales. The VOF model predictions showed excellent agreement with the generalized analytical solution by Mikic et al. [67], that accounts for both the inertia-controlled and the diffusion heat transfer-controlled stages of bubble growth, for all the examined scales and working fluids.

As a second step, more realistic cases of single bubble growth from superheated plates under saturated pool boiling conditions for both uniform and variable wettability characteristics as well as for complete bubble growth cycles up to detachment were considered for water and ethanol as working fluids, respectively. Once more, the applicability of the VOF model was explored for three progressively smaller scales. The overall results indicated that the utilized VOF-based numerical simulation framework provided results with reasonable physical interpretation even for spatial and temporal scales where up to now only mesoscale numerical simulation frameworks have been applied in the literature.

Summarizing, the present investigation demonstrates that the proposed enhanced VOF-based numerical simulation framework can be safely applied to significantly lower spatial and temporal scales that lie within the applicability limits of mesoscale numerical frameworks such as the FDI method. This is an important first step that can lead to the

coupling of these two powerful numerical approaches into a comprehensive multi-scale numerical framework for the modelling of boiling heat transfer, enabling the complete and physically accurate description of boiling heat transfer from bubble nucleation up to bubble detachment and bubble to bubble interaction that can result in an accurate prediction of boiling two-phase flow regimes without any empirical inputs.

CRediT authorship contribution statement

Bhaskar Chakraborty: Writing – original draft, Visualization, Validation, Software, Methodology, Investigation, Formal analysis, Data curation, Conceptualization. **Mirko Gallo:** Writing – review & editing, Supervision. **Marco Marengo:** Writing – review & editing, Supervision, Conceptualization. **Joel De Coninck:** Writing – review & editing, Conceptualization. **Carlo Massimo Casciola:** Writing – review & editing, Conceptualization. **Nicolas Miche:** Writing – review & editing, Supervision. **Anastasios Georgoulas:** Writing – review & editing, Writing – original draft, Validation, Supervision, Software, Resources, Project administration, Methodology, Investigation, Funding acquisition, Conceptualization.

Declaration of competing interest

The authors declare the following financial interests/personal relationships which may be considered as potential competing interests:

Anastasios Georgoulas reports financial support was provided by Leverhulme Trust. If there are other authors, they declare that they have no known competing financial interests or personal relationships that could have appeared to influence the work reported in this paper.

Data availability

Data will be made available on request.

Acknowledgements

The Authors would like to acknowledge that the preset investigation is fully funded by the UK Leverhulme Trust Fund grant AMUSe “Advanced MUltiscale stochastic Simulations of phase transition” RPG-2021–262.

References

[1] S. Nukiyama, The maximum and minimum values of the heat Q transmitted from metal to boiling water under atmospheric pressure, Int. J. Heat Mass Transf. 9 (12) (1966) 1419–1433, https://doi.org/10.1016/0017-9310(66)90138-4.
[2] R.A. Nelson, Do we doubt too little? Examples from the thermal sciences, Exp. Therm. Fluid Sci. 25 (5) (2001) 255–267, https://doi.org/10.1016/S0894-1777(01)00073-5.
[3] A. Hens, R. Agarwal, G. Biswas, Nanoscale study of boiling and evaporation in a liquid Ar film on a Pt heater using molecular dynamics simulation, Int. J. Heat Mass Transf. 71 (2014) 303–312, https://doi.org/10.1016/j.ijheatmasstransfer.2013.12.032.
[4] G. Nagayama, T. Tsuruta, P. Cheng, Molecular dynamics simulation on bubble formation in a nanochannel, Int. J. Heat Mass Transf. 49 (23–24) (2006) 4437–4443, https://doi.org/10.1016/j.ijheatmasstransfer.2006.04.030.
[5] S. Maruyama, T. Kimura, A Molecular dynamics simulation of bubble nucleation on solid surface, Trans. Jpn. Soc. Mech. Eng. Ser. B 65 (638) (1999) 3461–3467, https://doi.org/10.1299/kikaib.65.3461.
[6] T. Yamamoto, M. Matsumoto, Initial stage of nucleate boiling: molecular dynamics investigation, J. Therm. Sci. Technol. 7 (1) (2012) 334–349, https://doi.org/10.1299/jtst.7.334.
[7] W. Zhou, Y. Li, M. Li, J. Wei, W. Tao, Bubble nucleation over patterned surfaces with different wettabilities: molecular dynamics investigation, Int. J. Heat Mass Transf. 136 (2019) 1–9, https://doi.org/10.1016/j.ijheatmasstransfer.2019.02.093.
[8] Y.-J. Chen, B. Yu, Y. Zou, B.-N. Chen, W.-Q. Tao, Molecular dynamics studies of bubble nucleation on a grooved substrate, Int. J. Heat Mass Transf. 158 (2020) 119850, https://doi.org/10.1016/j.ijheatmasstransfer.2020.119850.
[9] H. Yu, Z. Li, Y. Tao, J. Sha, Y. Chen, Thermal bubble nucleation in graphene nanochannels, J. Phys. Chem. C 123 (6) (2019) 3482–3490, https://doi.org/10.1021/acs.jpcc.8b09038.
[10] N. Wu, L. Zeng, T. Fu, Z. Wang, C. Lu, Molecular dynamics study of rapid boiling of thin liquid water film on smooth copper surface under different wettability conditions, Int. J. Heat Mass Transf. 147 (2020) 118905, https://doi.org/10.1016/j.ijheatmasstransfer.2019.118905.
[11] B. Li, Y. Gu, M. Chen, Cavitation inception of water with solid nanoparticles: a molecular dynamics study, Ultrason. Sonochem. 51 (2019) 120–128, https://doi.org/10.1016/j.ultsonch.2018.10.036.
[12] T. Fu, Y. Mao, Y. Tang, Y. Zhang, W. Yuan, Effect of nanostructure on rapid boiling of water on a hot copper plate: a molecular dynamics study, Heat Mass Transf. 52 (8) (2016) 1469–1478, https://doi.org/10.1007/s00231-015-1668-2.
[13] J.C.F. Toledano, J. De Coninck, F. Dunlop, T. Huillet, How heterogeneous wettability enhances boiling, Physica A Stat. Mech. Appl. 622 (2023) 128847, https://doi.org/10.1016/j.physa.2023.128847.
[14] J. Diemand, R. Angélil, K.K. Tanaka, H. Tanaka, Direct simulations of homogeneous bubble nucleation: agreement with classical nucleation theory and no local hot spots, Phys. Rev. E 90 (5) (2014) 052407, https://doi.org/10.1103/PhysRevE.90.052407.
[15] M. Gallo, F. Magaletti, C.M. Casciola, Thermally activated vapor bubble nucleation: the Landau-Lifshitz–Van der Waals approach, Phys. Rev. Fluids 3 (5) (2018) 053604, https://doi.org/10.1103/PhysRevFluids.3.053604.
[16] M. Gallo, F. Magaletti, C.M. Casciola, Heterogeneous bubble nucleation dynamics, J. Fluid Mech. 906 (2021) A20, https://doi.org/10.1017/jfm.2020.761.
[17] F. Magaletti, M. Gallo, C.M. Casciola, Water cavitation from ambient to high temperatures, Sci. Rep. 11 (1) (2021) 20801, https://doi.org/10.1038/s41598-021-99863-z.
[18] D. Abbondanza, M. Gallo, C.M. Casciola, Diffuse interface modeling of laser-induced nano-/micro-cavitation bubbles, Phys. Fluids 35 (2) (2023), https://doi.org/10.1063/5.0136525.
[19] S. Mukherjee, H. Gomez, Effect of dissolved gas on the tensile strength of water, Phys. Fluids 34 (12) (2022), https://doi.org/10.1063/5.0131165.
[20] B. Barker, J.B. Bell, A.L. Garcia, Fluctuating hydrodynamics and the Rayleigh–Plateau instability, Proc. Natl. Acad. Sci. 120 (30) (2023), https://doi.org/10.1073/pnas.2306088120.
[21] F. Magaletti, M. Gallo, S.P. Perez, J.A. Carrillo, S. Kalliadasis, A positivity-preserving scheme for fluctuating hydrodynamics, J. Comput. Phys. 463 (2022) 111248, https://doi.org/10.1016/j.jcp.2022.111248.
[22] M. Bottacchiari, M. Gallo, M. Bussoletti, C.M. Casciola, The local variation of the Gaussian modulus enables different pathways for fluid lipid vesicle fusion, Sci. Rep. 14 (1) (2024) 23, https://doi.org/10.1038/s41598-023-50922-7.
[23] M. Bottacchiari, M. Gallo, M. Bussoletti, C.M. Casciola, Activation energy and force fields during topological transitions of fluid lipid vesicles, Commun. Phys. 5 (1) (2022) 283, https://doi.org/10.1038/s42005-022-01055-2.
[24] K.R. Elder, N. Provatas, J. Berry, P. Stefanovic, M. Grant, Phase-field crystal modeling and classical density functional theory of freezing, Phys. Rev. B 75 (6) (2007) 064107, https://doi.org/10.1103/PhysRevB.75.064107.
[25] R.F. Fox, G.E. Uhlenbeck, Contributions to non-equilibrium thermodynamics. I. Theory of hydrodynamical fluctuations, Phys. Fluids 13 (8) (1970) 1893–1902, https://doi.org/10.1063/1.1693183.
[26] F. Magaletti, A. Georgoulas, M. Marengo, Unraveling low nucleation temperatures in pool boiling through fluctuating hydrodynamics simulations, Int. J. Multiphase Flow 130 (2020) 103356, https://doi.org/10.1016/j.ijmultiphaseflow.2020.103356.
[27] M. Gallo, F. Magaletti, D. Cocco, C.M. Casciola, Nucleation and growth dynamics of vapour bubbles, J. Fluid Mech. 883 (2020) A14, https://doi.org/10.1017/jfm.2019.844.
[28] M. Gallo, Thermal fluctuations in metastable fluids, Phys. Fluids 34 (12) (2022), https://doi.org/10.1063/5.0132478.
[29] M. Gallo, F. Magaletti, A. Georgoulas, M. Marengo, J. De Coninck, C.M. Casciola, A nanoscale view of the origin of boiling and its dynamics, Nat. Commun. 14 (1) (2023) 6428, https://doi.org/10.1038/s41467-023-41959-3.
[30] C.W. Hirt, B.D. Nichols, Volume of fluid (VOF) method for the dynamics of free boundaries, J. Comput. Phys. 39 (1) (1981) 201–225, https://doi.org/10.1016/0021-9991(81)90145-5.
[31] S. Saincher, S. V, An efficient operator-split CICSAM scheme for three-dimensional multiphase-flow problems on Cartesian grids, Comput. Fluids 240 (2022) 105440, https://doi.org/10.1016/j.compfluid.2022.105440.
[32] B. Chakraborty, J. Banerjee, A sharpness preserving scheme for interfacial flows, Appl. Math. Model. 40 (21–22) (2016) 9398–9426, https://doi.org/10.1016/j.apm.2016.06.012.
[33] H.K. Zinjala, J. Banerjee, A Lagrangian-Eulerian advection scheme with moment-of-fluid interface reconstruction, Numer. Heat Transf. Part B Fundam. 69 (6) (2016) 563–574, https://doi.org/10.1080/10407790.2016.1138753.
[34] M. Andredaki, K. Vontas, A. Georgoulas, N. Miché, M. Marengo, The effect of channel aspect ratio on flow boiling characteristics within rectangular micro-passages, Int. J. Heat Mass Transf. 183 (2022), https://doi.org/10.1016/j.ijheatmasstransfer.2021.122201.
[35] K. Vontas, M. Andredaki, A. Georgoulas, N. Miché, M. Marengo, The effect of surface wettability on flow boiling characteristics within microchannels, Int. J. Heat Mass Transf. 172 (2021) 121133, https://doi.org/10.1016/j.ijheatmasstransfer.2021.121133.
[36] K. Vontas, N. Miché, M. Marengo, A. Georgoulas, A numerical investigation of the solid surface material influence on flow boiling within microchannels, Appl.

Therm. Eng. 217 (2022) 119006, https://doi.org/10.1016/j.applthermaleng.2022.119006.
[37] A. Georgoulas, M. Andredaki, M. Marengo, An enhanced VOF method coupled with heat transfer and phase change to characterise bubble detachment in saturated pool boiling, Energies (Basel) 10 (3) (2017) 272, https://doi.org/10.3390/en10030272.
[38] S.W.J. Welch, T. Rachidi, Numerical computation of film boiling including conjugate heat transfer, Numer. Heat Transf. Part B Fundam. 42 (1) (2002) 35–53, https://doi.org/10.1080/10407790190053824.
[39] S.W.J. Welch, J. Wilson, A volume of fluid based method for fluid flows with phase change, J. Comput. Phys. 160 (2) (2000) 662–682, https://doi.org/10.1006/jcph.2000.6481.
[40] S. Aus der Wiesche, Bubble growth and departure during nucleate boiling: the occurrence of heat flux reversal, in: Proceedings of the 4th International Conference on Computational Heat and Mass Transfer, 2005. Paris.
[41] S. Hardt, F. Wondra, Evaporation model for interfacial flows based on a continuum-field representation of the source terms, J. Comput. Phys. 227 (11) (2008) 5871–5895, https://doi.org/10.1016/j.jcp.2008.02.020.
[42] O.S.E. Yasuo, K. Tomoaki, Numerical study on subcooled pool boiling, in: Progress in Nuclear Science And Technology, 2011, pp. 125–129. Kyoto.
[43] Y. Ose, T. Kunugi, Development of a boiling and condensation model on subcooled boiling phenomena, Energy Procedia 9 (2011) 605–618, https://doi.org/10.1016/j.egypro.2011.09.071.
[44] C. Kunkelmann, K. Ibrahem, N. Schweizer, S. Herbert, P. Stephan, T. Gambaryan-Roisman, The effect of three-phase contact line speed on local evaporative heat transfer: experimental and numerical investigations, Int. J. Heat Mass Transf. 55 (7–8) (2012) 1896–1904, https://doi.org/10.1016/j.ijheatmasstransfer.2011.11.044.
[45] C. Kunkelmann, P. Stephan, CFD simulation of boiling flows using the volume-of-fluid method within OpenFOAM, Numer. Heat Transf. A Appl. 56 (8) (2009) 631–646, https://doi.org/10.1080/10407780903423908.
[46] C. Kunkelmann, Numerical Modeling and Investigation of Boiling Phenomena, 2011. Ph.D. Thesis, Technical University of Darmstadt, https://tuprints.ulb.tu-darmstadt.de/2731/1/PhD_Thesis_Kunkelmann.pdf.
[47] Y. Sato, B. Ničeno, A sharp-interface phase change model for a mass-conservative interface tracking method, J. Comput. Phys. 249 (2013) 127–161, https://doi.org/10.1016/j.jcp.2013.04.035.
[48] M. Andredaki, A. Georgoulas, N. Miché, M. Marengo, Break-up mechanisms and conditions for vapour slugs within mini-channels, in: 15th UK Heat Transfer Conference, UKHTC2017, Brunel University London, 4-5 September 2017, 2017.
[49] M. Andredaki, K. Vontas, A. Georgoulas, N. Miché, M. Marengo, The effect of channel aspect ratio on flow boiling characteristics within rectangular micro-passages, Int. J. Heat Mass Transf. 183 (2022) 122201, https://doi.org/10.1016/j.ijheatmasstransfer.2021.122201.
[50] K. Vontas, M. Andredaki, A. Georgoulas, N. Miché, M. Marengo, The effect of surface wettability on flow boiling characteristics within microchannels, Int. J. Heat Mass Transf. 172 (2021) 121133, https://doi.org/10.1016/j.ijheatmasstransfer.2021.121133.
[51] K. Vontas, M. Andredaki, A. Georgoulas, N. Miché, M. Marengo, The effect of hydraulic diameter on flow boiling within single rectangular microchannels and comparison of heat sink configuration of a single and multiple microchannels, Energies (Basel) 14 (20) (2021) 6641, https://doi.org/10.3390/en14206641.
[52] K. Vontas, N. Miché, M. Marengo, A. Georgoulas, A numerical investigation of the solid surface material influence on flow boiling within microchannels, Appl. Therm. Eng. 217 (2022) 119006, https://doi.org/10.1016/j.applthermaleng.2022.119006.
[53] M. Andredaki, A. Georgoulas, N. Miché, M. Marengo, Accelerating Taylor bubbles within circular capillary channels: break-up mechanisms and regimes, Int. J. Multiphase Flow 134 (Jan. 2021) 103488, https://doi.org/10.1016/j.ijmultiphaseflow.2020.103488.
[54] M. Andredaki, A. Georgoulas, N. Miche, M. Marengo, Numerical investigation of liquid film instabilities and evaporation in confined oscillating slug-plug flows, in: WIT Transactions on Engineering Sciences, Computational and Experimental Methods in Multiphase and Complex Flow X, 2019.
[55] J.U. Brackbill, D.B. Kothe, C. Zemach, A continuum method for modeling surface tension, J. Comput. Phys. 100 (2) (1992) 335–354, https://doi.org/10.1016/0021-9991(92)90240-Y.
[56] D.A. Hoang, V. van Steijn, L.M. Portela, M.T. Kreutzer, C.R. Kleijn, Benchmark numerical simulations of segmented two-phase flows in microchannels using the Volume of Fluid method, Comput. Fluids. 86 (2013) 28–36, https://doi.org/10.1016/j.compfluid.2013.06.024.
[57] S.S. Deshpande, L. Anumolu, M.F. Trujillo, Evaluating the performance of the two-phase flow solver interFoam, Comput. Sci. Discov. 5 (1) (2012) 14016, https://doi.org/10.1088/1749-4699/5/1/014016.
[58] A. Georgoulas, P. Koukouvinis, M. Gavaises, M. Marengo, Numerical investigation of quasi-static bubble growth and detachment from submerged orifices in isothermal liquid pools: the effect of varying fluid properties and gravity levels, Int. J. Multiphase Flow 74 (2015) 59–78, https://doi.org/10.1016/j.ijmultiphaseflow.2015.04.008.
[59] C. Greenshields, OpenFOAM v10 User Guide, CFD Direct, 2012.
[60] R. Scardovelli, S. Zaleski, Direct numerical simulation of free-surface and interfacial flow, Annu. Rev. Fluid Mech. 31 (1) (1999) 567–603, https://doi.org/10.1146/annurev.fluid.31.1.567.
[61] D.A. Hoang, V. van Steijn, L.M. Portela, M.T. Kreutzer, C.R. Kleijn, Benchmark numerical simulations of segmented two-phase flows in microchannels using the Volume of Fluid method, Comput. Fluids 86 (2013) 28–36, https://doi.org/10.1016/j.compfluid.2013.06.024.
[62] R.W. Schrage, A Theoretical Study of Interphase Mass Transfer, Columbia University Press, 1953, https://doi.org/10.7312/schr90162.
[63] C. Kunkelmann, P. Stephan, Numerical simulation of the transient heat transfer during nucleate boiling of refrigerant HFE-7100, Int. J. Refrig. 33 (7) (2010) 1221–1228, https://doi.org/10.1016/j.ijrefrig.2010.07.013.
[64] M. Mirco, CFD modeling of two-phase boiling flows in the slug flow regime with an interface capturing technique (2012). Ph.D. Thesis, University of Bologna. https://amsdottorato.unibo.it/4437/1/Magnini_Mirco_tesi.pdf.
[65] M.S. Plesset, S.A. Zwick, The growth of vapor bubbles in superheated liquids, J. Appl. Phys. 25 (4) (1954) 493–500, https://doi.org/10.1063/1.1721668.
[66] L.E. Scriven, On the dynamics of phase growth, Chem. Eng. Sci. 50 (24) (1995) 3905, https://doi.org/10.1016/0009-2509(96)81820-3.
[67] B.B. Mikic, W.M. Rohsenow, P. Griffith, On bubble growth rates, Int. J. Heat Mass Transf. 13 (4) (1970) 657–666, https://doi.org/10.1016/0017-9310(70)90040-2.
[68] E. Teodori, P. Pontes, A. Moita, A. Georgoulas, M. Marengo, A. Moreira, Sensible heat transfer during droplet cooling: experimental and numerical analysis, Energies (Basel) 10 (6) (2017) 790, https://doi.org/10.3390/en10060790.
[69] P. Pontes, I. Gonçalves, M. Andredaki, A. Georgoulas, A.L.N. Moreira, A.S. Moita, Fluid flow and heat transfer in microchannel devices for cooling applications: experimental and numerical approaches, Appl. Therm. Eng. 218 (2023) 119358, https://doi.org/10.1016/j.applthermaleng.2022.119358.
[70] D.J. Bouchard, M. Andredaki, A. Georgoulas, M. Marengo, S. Chandra, Penetration characteristics of a liquid droplet impacting on a narrow gap: experimental and numerical analysis, Phys. Fluids 34 (5) (2022) 57111, https://doi.org/10.1063/5.0091045.
[71] P. Pontes, R. Cautela, E. Teodori, A.S. Moita, A. Georgoulas, A.L.N.M. Moreira, Bubble dynamics and heat transfer on biphilic surfaces: experiments and numerical simulation, J. Bionic. Eng. 17 (4) (2020) 809–821, https://doi.org/10.1007/s42235-020-0064-x.